nature medicine

ARTICLES

https://doi.org/10.1038/s41591-019-0423-5

Corrected: Publisher Correction

Methionine is a metabolic dependency of tumor-initiating cells

Zhenxun Wang[1,11], Lian Yee Yip[2,11], Jia Hui Jane Lee[1,3], Zhengwei Wu[1,4], Hui Yi Chew[1], Pooi Kiat William Chong[2], Chin Chye Teo[2], Heather Yin-Kuan Ang[1], Kai Lay Esther Peh[2], Ju Yuan[1], Siming Ma[1], Li Shi Kimberly Choo[1], Nurhidayah Basri[2], Xia Jiang[1], Qiang Yu[1], Axel M. Hillmer[1], Wan Teck Lim[5,6,7], Tony Kiat Hon Lim[8], Angela Takano[8], Eng Huat Tan[5], Daniel Shao Weng Tan[1,5], Ying Swan Ho[2], Bing Lim[9*] and Wai Leong Tam[1,3,4,10*]

Understanding cellular metabolism holds immense potential for developing new classes of therapeutics that target metabolic pathways in cancer. Metabolic pathways are altered in bulk neoplastic cells in comparison to normal tissues. However, carcinoma cells within tumors are heterogeneous, and tumor-initiating cells (TICs) are important therapeutic targets that have remained metabolically uncharacterized. To understand their metabolic alterations, we performed metabolomics and metabolite tracing analyses, which revealed that TICs have highly elevated methionine cycle activity and transmethylation rates that are driven by MAT2A. High methionine cycle activity causes methionine consumption to far outstrip its regeneration, leading to addiction to exogenous methionine. Pharmacological inhibition of the methionine cycle, even transiently, is sufficient to cripple the tumor-initiating capability of these cells. Methionine cycle flux specifically influences the epigenetic state of cancer cells and drives tumor initiation. Methionine cycle enzymes are also enriched in other tumor types, and MAT2A expression impinges upon the sensitivity of certain cancer cells to therapeutic inhibition.

Cancer-specific metabolism represents an area with therapeutic potential as cancer cells depend on altered metabolic states for tumor proliferation and stress adaptation[1–10]. Mutations in genes encoding multiple tricarboxylic acid (TCA) cycle enzymes, including *IDH1* and *IDH2*, have also been shown to drive specific cancers, while *PHGDH*, the gene encoding the first enzyme of the serine–glycine pathway, is amplified in melanoma and crucial for proliferation of melanoma and breast cancer cells[11,12]. These alterations invariably inhibit downstream DNA and histone demethylases, resulting in hypermethylation of DNA and histones, emphasizing the significance of metabolic processes in epigenetic modifications that promote tumorigenesis[13–17].

The majority of studies have focused on parsing the metabolic disparity between bulk tumor and normal cells. Solid tumors are highly heterogeneous, containing diverse intratumoral subpopulations of neoplastic cells[18,19]. Among these are TICs (also termed cancer stem cells) that are responsible for tumor initiation. TICs are often resistant to conventional chemotherapy, thereby favoring relapse into more aggressive cancers, and they also appear to be highly invasive and metastatic[20,21]. These observations underscore the unexplored impact of developing therapies that target TICs[22,23].

Because TICs functionally differ from non-TICs, they exhibit distinct metabolic requirements. Glycine decarboxylase (GLDC), an enzyme in the serine–glycine pathway, is overexpressed in lung TICs to support their proliferation by redirecting the fluxes in downstream metabolic processes, but it remains unclear which relevant metabolites are involved[24]. To gather insights, we performed unbiased liquid chromatography and mass spectrometry (LC–MS) analysis and found methionine cycle substrates to be strikingly enriched in TICs in comparison to corresponding non-TICs derived through using specific cell culture conditions. By using isotopic label tracing, TICs were found to exhibit high methionine cycle flux and a remarkable dependency on exogenous methionine, but not other amino acids. Transient pharmacological inhibition of methionine cycle enzymes was sufficient to result in long-term loss of tumorigenic potential. This was largely attributed to alterations in cellular methylation that resulted from depletion of *S*-adenosyl methionine (SAM), an essential and universal substrate for transmethylation reactions[25–27]. Our results demonstrate the rate-limiting role of the methionine cycle in tumorigenesis, thereby providing new insights into metabolic vulnerabilities in lung cancer.

Results

Metabolomic comparison of patient-derived lung tumor-initiating cells and isogenic differentiated cells. To dissect the role of metabolic alterations in TICs, we used two previously characterized TIC-enriched lines (LC10 and LC32) derived from resected primary non-small-cell lung cancer (NSCLC) adenocarcinoma samples and grown as non-adherent tumorspheres (TS; TS10 and TS32) in serum-free medium (Fig. 1a)[24]. These tumorsphere lines

[1]Genome Institute of Singapore, Agency for Science, Technology and Research (A*STAR), Singapore, Singapore. [2]Bioprocessing Technology Institute, Agency for Science, Technology and Research (A*STAR), Singapore, Singapore. [3]School of Biological Sciences, Nanyang Technological University, Singapore, Singapore. [4]Cancer Science Institute of Singapore, National University of Singapore, Singapore, Singapore. [5]Division of Medical Oncology, National Cancer Centre Singapore, Singapore, Singapore. [6]Institute of Molecular and Cell Biology, Agency for Science, Technology and Research (A*STAR), Singapore, Singapore. [7]Duke-NUS Medical School, Singapore, Singapore. [8]Department of Anatomical Pathology, Singapore General Hospital, Singapore, Singapore. [9]Merck Sharp and Dohme Translational Medicine Research Centre, Singapore, Singapore. [10]Department of Biochemistry, Yong Loo Lin School of Medicine, National University of Singapore, Singapore, Singapore. [11]These authors contributed equally: Zhenxun Wang, Lian Yee Yip.
*e-mail: bing.lim@merck.com; tamwl@gis.a-star.edu.sg

are highly tumorigenic, as demonstrated by their in vitro colony-forming potential and their ability to form tumors when subcutaneously implanted into immune-compromised NOD.Cg-*Prkdc*^{scid} *Il2rg*^{tm1Wjl}/SzJ (NSG) mice at limiting-dilution cell frequencies (Fig. 1b–d and Extended Data Fig. 1a). Resultant xenograft tumors bore molecular and histological resemblance to their parental tumors and were heterogeneous with respect to expression of CD166 (a TIC surface marker), thereby demonstrating the derivation of non-TICs from TICs[24] (Supplementary Table 1 and Extended Data Fig. 1b).

From each of these parental tumorsphere cell lines, two types of corresponding isogenic cell lines were derived by using special culture conditions. First, adherent (Adh; Adh10 and Adh32) cells were generated by continual passage in serum-containing medium. Second, stable *GLDC*-knockdown lines were generated by using shRNA hairpins against *GLDC* (*GLDC* KD; GLDC10 and GLDC32) and grown under parental tumorsphere medium conditions[24]. Both adherent and *GLDC*-knockdown cells showed a decrease in CD166 cell-surface expression and were dramatically less tumorigenic in comparison to parental tumorspheres, forming very few colonies in soft agar and producing very small tumors in NSG mice (Fig. 1b,c and Extended Data Fig. 1a,b). Limiting-dilution assays demonstrated at least a 40-fold decrease in TIC frequency in adherent and *GLDC*-knockdown lines in comparison to the parental tumorsphere cells (Fig. 1d). Strikingly, the in vitro proliferation rates of these isogenic cell lines did not correlate with tumor-initiation potential (Extended Data Fig. 1c). Adherent cells, in fact, grew faster than both tumorsphere and *GLDC*-knockdown cells, underscoring the decoupling of cell proliferation in vitro from tumorigenicity. Thus, tumorsphere cells were greatly enriched for TICs, whereas adherent and *GLDC*-knockdown cells were largely composed of non-TICs with high proliferative capacity but limited tumorigenic potential.

To determine the abundance of specific metabolites in the three cell lines derived from TS32 (tumorsphere, adherent and *GLDC* knockdown), we performed an unbiased LC–MS-based metabolomic analysis (Fig. 1e and Supplementary Table 2). Glycolytic intermediates were enriched in adherent cells relative to tumorspheres and *GLDC*-knockdown cells, which is attributable to the higher rates of proliferation in adherent cells (Extended Data Fig. 1c). Lactate levels were lower in *GLDC*-knockdown cells, when compared to adherent and tumorsphere cells, in line with our previous study[24]. Although lactate levels were comparable between adherent cells and tumorspheres, glycolysis stress tests indicated that adherent cells had higher basal and maximal extracellular acidification rates (ECARs), suggesting that glycolytic flux was higher in these cells (Extended Data Fig. 1d). The abundance of metabolites in control-knockdown cells and *GLDC*-knockdown cells stably expressing shRNA-resistant *GLDC* cDNA was concordant with that in parental TS32 cells, ruling out the possibility that differences in metabolite abundance were due to off-target effects of the shRNAs (Supplementary Table 3).

From the global metabolomic analysis, three classes of metabolites stood out: (i) nucleotide intermediates, derived from activity of the serine–glycine and one-carbon pathways, whose enrichments were observed in tumorsphere cells but were abrogated by *GLDC* knockdown[3,24]; (ii) branched-chain and aromatic amino acids; and (iii) metabolites related to the methionine cycle (Fig. 1e). We chose to focus on the methionine cycle because it represents a highly defined metabolic module in which key metabolites, such as methionine, SAM and *S*-adenosyl homocysteine (SAH), were strongly enriched in tumorspheres and contribution of the methionine cycle to tumor initiation has not previously been established (Fig. 1f–h). The methionine cycle is composed of two main steps (Fig. 1f). In the first step, methionine adenosyltransferase II alpha (MAT2A) consumes methionine and ATP to generate SAM—a universal methyl-group donor in cells. SAH is produced as a by-product of methylation reactions. The second step regenerates methionine via reversible conversion of SAH to homocysteine by SAH hydrolase (SAHH). Methionine is subsequently resynthesized from homocysteine by using methyl-tetrahydrofolate (CH_3-THF) as a methyl donor; this is catalyzed by methionine synthase (MTR).

In adherent and *GLDC*-knockdown cells, methionine and SAH were consistently depleted in comparison to their levels in tumorspheres, suggesting that decreases in methionine cycle activity and cellular transmethylation were associated with the lack of tumor-initiating capability (Fig. 1g). Protein levels of GLDC, serine hydroxymethyltransferase 2 (SHMT2) and methylenetetrahydrofolate reductase (MTHFR) were much higher in tumorspheres than in adherent cells, and MTHFR levels were higher in control-knockdown tumorsphere cells than in *GLDC*-knockdown cells (Fig. 1i). Both results are consistent with the observation that nucleotide pools, which are derived from one-carbon metabolites, were much larger in tumorspheres than in adherent or *GLDC*-knockdown cells

Fig. 1 | Metabolomic characterization of lung tumor-initiating cells and differentiated cells. a, Two cell lines were derived from tumorspheres (TS; left): adherent cells (Adh; top right) that were generated by continual passaging of tumorspheres in serum-supplemented tumorsphere medium without growth factors and tumorspheres transduced with an shRNA hairpin against *GLDC* (*GLDC* KD; bottom right). White bar, 20 µm. **b**, Ability of tumorspheres, adherent cells and *GLDC*-knockdown cells to form colonies in soft agar. Shown is the mean number of crystal-violet-stained colonies after 2 months; 5,000 cells were plated per well. Error bars, s.d.; $n = 4$ biologically independent experiments. **c**, Mean volume of tumors seeded with 500,000 cells of the indicated type. Error bars, s.e.m.; $n = 4$ tumors. **d**, Top, frequency of TICs in tumorspheres, *GLDC*-knockdown cells and adherent cells. Frequency was calculated by using the ELDA software program (http://bioinf.wehi.edu.au/software/elda/). LTIC, lung tumor-initiating cell; CI, confidence interval. *P* values were generated with the chi-squared goodness-of-fit test; d.f. = 1. Bottom, mean tumor weights following subcutaneous implantation of cells. Cell type and number are stated on the *x* axis; the number of tumors per injections is indicated above each bar. For injection with 10,000 and 100,000 cells, tumors were collected 8 weeks after implantation; tumors from injection of 500,000 cells were collected 6 weeks after implantation. Error bars, s.d. **e**, Metabolomic comparison of adherent, *GLDC*-knockdown and tumorsphere cells. Three biological replicates are shown as separate columns for each cell type. AA, amino acid. $\log_2$(ratio), $\log_2$ of the ratio between the metabolite abundance of each sample to the average abundance across all samples. **f**, Schematic of the serine–glycine and methionine cycle pathways. Metabolic enzymes are in red. **g**, Abundance of intracellular primary methionine cycle metabolites as determined by LC–MS, normalized to abundance in adherent cells. Data represent the mean ± s.d.; $^*P < 0.05$, $^{**}P < 0.01$, $^{***}P < 0.001$, determined by one-sided multiple *t* test with statistical significance corrected for multiple comparisons by the Holm–Sidak method; $n = 3$ biologically independent experiments. Exact *P* values are as follows: TS vs. Adh: methionine, 0.000628; SAM, 0.029975; SAH, 0.036574; TS vs. *GLDC* KD: methionine, 0.001942; SAH, 0.005839. **h**, Abundance of intracellular glutathione-associated metabolites as determined by LC–MS, normalized to abundance in adherent cells. Data represent the mean ± s.d.; $^{**}P < 0.01$, $^{***}P < 0.001$, determined by one-sided multiple *t* test with statistical significance corrected for multiple comparisons by the Holm–Sidak method; $n = 3$ biologically independent experiments. Exact *P* values are as follows: TS vs. Adh: GSH, 0.000071; glutamine, 0.00014; glutamate, 0.000035; TS vs. *GLDC* KD: GSH, 0.003416; glutamine, 0.003093; glutamate, 0.002652. **i**, Protein levels of metabolic enzymes in tumorspheres, adherent cells and *GLDC*-knockdown cells. β-actin was used as a loading control. Independent blots were repeated at least three times with similar results. sh, shRNA. **j**, Protein levels of modified histones in tumorspheres, adherent cells and *GLDC*-knockdown cells. Histone H3 was used as a loading control. Independent blots were repeated at least three times with similar results. See also Extended Data Fig. 1.

(Fig. 1e). Knockdown of *GLDC* led to a similar decrease in steady-state levels of ATP, a SAM precursor, as knockdown of *SHMT2* (Extended Data Fig. 1e)[28]. The decrease could be rescued by supplementing knockdown cells with formate, a cell-permeable one-carbon donor[28,29]. These findings are in agreement with the observation that *GLDC* knockdown led to decreased abundance of nucleotides and indicate that GLDC activity has a prominent role in TICs through one-carbon flux (Fig. 1e). These data show that GLDC suppression exerts an effect on ATP production via an impact on the one-carbon pool, in agreement with the hypothesis that the glycine cleavage complex is active in these cells.

In contrast, formate supplementation could not rescue the lower ATP levels in adherent cells, even when SHMT2 or GLDC was re-expressed (Extended Data Fig. 1f). Re-expression of GLDC in

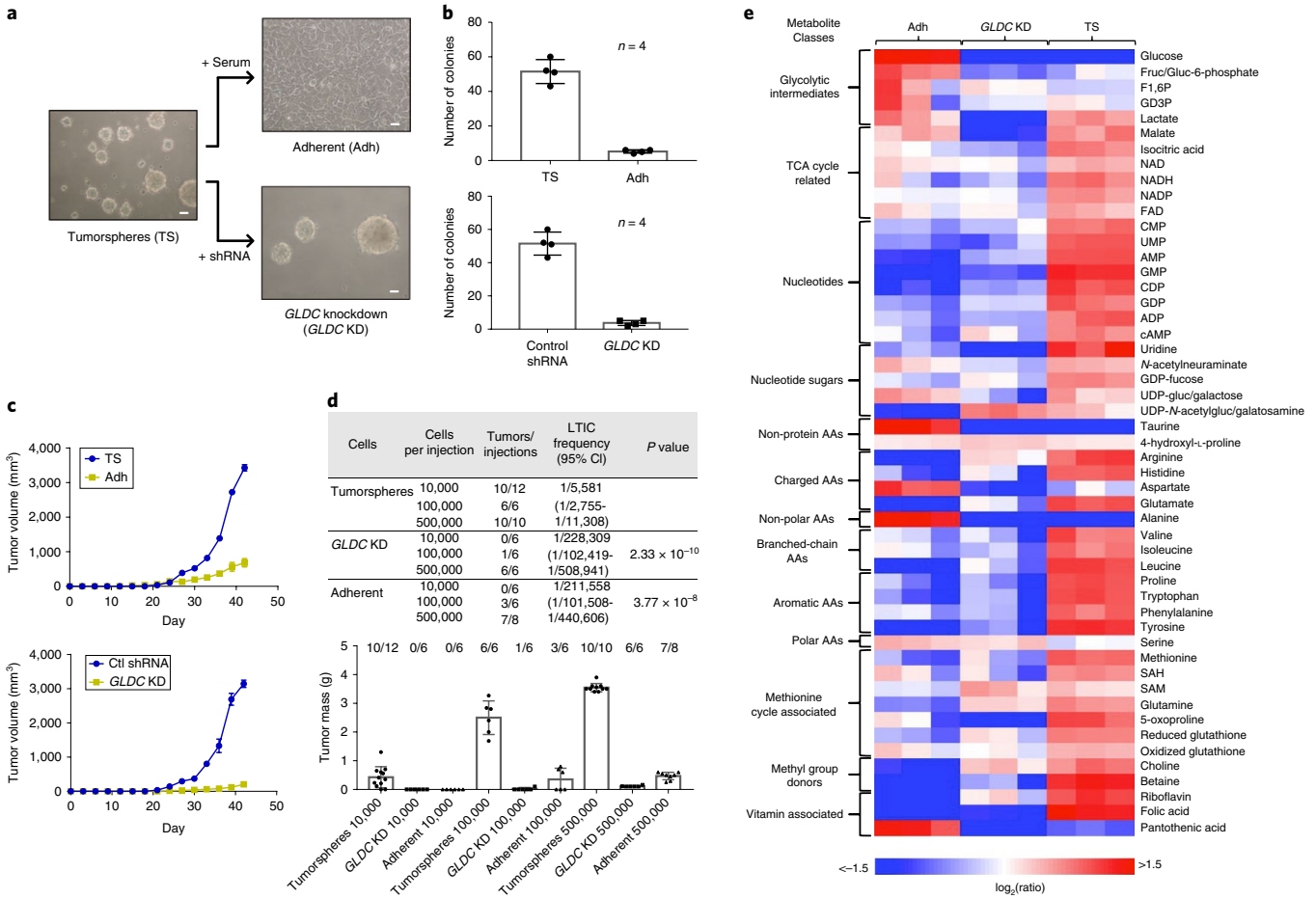

Cells	Cells per injection	Tumors/ injections	LTIC frequency (95% CI)	*P* value
Tumorspheres	10,000	10/12	1/5,581	
	100,000	6/6	(1/2,755-	
	500,000	10/10	1/11,308)	
GLDC KD	10,000	0/6	1/228,309	
	100,000	1/6	(1/102,419-	2.33×10^{-10}
	500,000	6/6	1/508,941)	
Adherent	10,000	0/6	1/211,558	
	100,000	3/6	(1/101,508-	3.77×10^{-8}
	500,000	7/8	1/440,606)	

adherent cells also failed to fully rescue the tumorigenic potential of these cells (Extended Data Fig. 1g). In addition, extended culture (~2 weeks) of adherent cells under tumorsphere medium conditions did not lead to recovery of CD1166$^+$ cells and/or final tumor load, indicating that the decrease in TIC state in adherent cells was permanent (Extended Data Fig. 1h,i). These data demonstrate the importance of the one-carbon pathway in contributing to the tumorigenicity of TICs.

Interestingly, there was no significant difference in SAM levels in *GLDC*-knockdown cells in comparison to tumorsphere cells, despite the decreased methionine levels in knockdown cells (Fig. 1g). This may best be explained by a decreased rate of cellular transmethylation reactions leading to lower levels of SAH. Although decreased levels of SAH in adherent and *GLDC*-knockdown cells might be the result of increased SAH consumption from glutathione synthesis, there was no evidence of this, with glutathione levels similarly decreased in adherent and *GLDC*-knockdown cells (Fig. 1h). To confirm that decreased SAH levels in non-TICs relative to TICs were due to reduced rates of transmethylation, we examined the abundance of methylated histones. In comparison to tumorsphere cells, the majority of histone methylated marks in both adherent and *GLDC*-knockdown cells were greatly downregulated (Fig. 1j). The abundance of methylated histones in adherent and tumorsphere cells was also insensitive to alterations in cell culture conditions, as tumorsphere cells grown transiently in adherent cell medium, and vice versa, did not have altered levels (Extended Data Fig. 1j).

To determine whether CD166$^+$ cells isolated from established tumorsphere-derived xenografted tumors also had elevated methionine cycle activity, we analyzed cells sorted on the basis of their cell-surface expression of CD166 (Extended Data Fig. 1k,l). In agreement with our in vitro observations, the methionine and SAM metabolites were enriched in CD166$^+$ cells relative to their CD166$^-$ counterparts (Extended Data Fig. 1k). CD166$^+$ cells also had higher abundance of methylated histones. The abundance of the MAT2A protein, whose expression is directly correlated with demand for methionine and SAM, was also higher (Extended Data Fig. 1l)[30–32].

Methionine is an indispensable metabolic substrate for lung tumor-initiating cells. To assess the specific importance of methionine cycle metabolites in tumorsphere cells, we performed a transient 48-h starvation protocol because the general lethality associated with long-term (>7-d) methionine depletion could confound our conclusions (Fig. 2a)[33,34]. Following this protocol, we immediately assessed its functional impact on cells in downstream assays performed under complete nutrient conditions. Methionine starvation for 48 h reduced methionine cycle activity, as exemplified by a dramatic decrease (~30-fold) in SAM levels and a slight decrease in SAH levels (Fig. 2b). This was accompanied by an overall decrease in histone methylation (Fig. 2c). Tumorsphere cells were assayed for their colony-forming ability in vitro and their in vivo tumorigenic potential when xenografted into NSG mice (Fig. 2d and Extended Data Fig. 2a). Unexpectedly, tumorsphere cells that were transiently deprived of methionine did not regain their colony-forming abilities despite being returned to non-starvation conditions during soft agar assays. Their in vivo tumor-forming ability was severely diminished, as evidenced by a dramatic decrease in tumor load of 94% (Fig. 2d,e and Extended Data Fig. 2a,b). Remarkably, shorter-term (24-h) starvation of tumorsphere cells was also sufficient to disrupt their tumorigenic potential, underscoring their absolute dependency on methionine for tumor initiation (Extended Data Fig. 2c). In line with this, we also observed a decrease in cell-surface expression of CD166 upon methionine starvation (Extended Data Fig. 2d).

Methionine is an essential amino acid. Hence, even short-term starvation may result in a general loss of cell viability that may be unrelated to tumor-initiation potential. To address this possibility, we transiently starved tumorsphere cells of other essential amino acids, including threonine, leucine or tryptophan, in a manner similar to starvation for methionine, before they were xenografted into NSG mice (Fig. 2f). Leucine and tryptophan were selected because they were enriched in tumorsphere cells (Fig. 1e), while threonine was previously documented to be important in influencing SAM levels in embryonic stem cells[27]. Transient starvation for these amino acids did not severely affect tumorigenic ability, and these cells remained viable and regained proliferation when they were returned to complete medium (Extended Data Fig. 2e).

To further confirm that the defects in colony- and tumor-forming ability were attributable to loss of methionine cycle activity, and not to a general loss of viability or translation inhibition, we tried to rescue methionine-starved cells through three approaches

Fig. 2 | The metabolic requirements of lung tumor-initiating cells. a, Schematic of metabolite starvation and downstream analyses. Tumorsphere cells were starved in medium lacking in one specific metabolite for 48 h. Experiments were carried out thereafter under non-starvation conditions. **b**, Abundance of methionine cycle metabolites 48 h after methionine starvation, as determined by LC–MS, with values normalized to abundance in the complete condition. Data represent means ± s.d.; $n = 3$. **c**, Western blot analyses of cells starved for the indicated metabolite for 48 h. Total histone H3 was used as a loading control. Independent blots were repeated at least three times with similar results. **d**, Effect of short-term metabolite starvation on TIC tumorigenicity. Shown is the mean volume of tumors seeded with 500,000 tumorsphere cells grown under the indicated conditions before injection. Error bars, s.e.m.; $n = 4$ tumors. The growth curve for tumorsphere cells grown under the complete condition in Fig. 1c is included for comparison. **e**, Left, mean tumor mass following subcutaneous implantation of cells. The starvation condition and number of cells are stated on the *x* axis; the number of injections is indicated above each bar. For injection of 10,000 and 100,000 cells, tumors were collected 8 weeks after implantation; tumors from injection of 500,000 cells were collected 6 weeks after implantation. Error bars, s.d. Right, frequency of TICs present in tumorsphere cells and methionine-starved tumorsphere cells. Frequency was calculated by using the ELDA program. The *P* value was generated with the chi-squared goodness-of-fit test; d.f. = 1. **f**, Mean tumor mass in NSG mice following transplantation of 500,000 cells previously starved for 48 h. Starvation conditions are indicated on the *x* axis. Error bars, s.d.; $n = 5$ tumors for leucine, tryptophan and threonine starvation, $n = 9$ tumors for methionine and serine/glycine starvation, and $n = 6$ tumors for glutamine starvation and the complete condition. $^*P < 0.05$, $^{**}P < 0.01$, $^{****}P < 0.001$, determined by using the unpaired two-sided Student's *t* test with Welch's correction. Exact *P* values are as follows: complete vs. no leucine, $P < 0.001$; complete vs. no tryptophan, 0.9698; complete vs. no threonine, 0.0082; complete vs. no serine and glycine, $P < 0.001$; complete vs. no glutamine, 0.0177; complete vs. no methionine, $P < 0.001$. **g**, Western blot analyses of cells in the presence or absence of specific metabolites. Total histone H3 was used as a loading control. Independent blots were repeated at least three times with similar results. Cells were starved for 48 h for methionine but supplemented with homocysteine (HCY; 250 μM), SAM (500 μM) or replated into complete medium for the next 48 h (48/48). **h**, Effect of the presence or absence of specific metabolites on the colony- and tumor-forming abilities of tumorsphere cells. Shown is the mean volume of tumors seeded with 500,000 tumorsphere cells grown under the indicated conditions before injection. Error bars, s.e.m.; $n = 4$ tumors. Growth curves for tumorsphere cells grown under the complete condition in Fig. 1c and the methionine starvation condition in **d** are included for comparison. **i**, Assessment of apoptosis in metabolite-starved cells. Left, flow cytometry plots of tumorsphere cells stained with Annexin V-FITC/PI. Cells treated with 10 mM hydrogen peroxide for 48 h served as a positive control. Right, mean percentage of Annexin V$^+$ cells. Error bars, s.d.; $n = 4$. See also Extended Data Fig. 2.

(Fig. 2g,h and Extended Data Fig. 2f). First, we supplemented methionine starvation medium with 250 µM homocysteine to determine whether tumorsphere cells could use homocysteine to regenerate methionine. Second, we supplemented methionine starvation medium with 500 µM SAM to directly bypass the requirement of methionine for methylation. Third, we recovered methionine-starved tumorsphere cells for 48 h in complete medium before functional assessment.

To dissect changes to methionine cycle activity under these three rescue conditions, we first analyzed cellular histone methylation (Fig. 2g). When methionine-starved tumorsphere cells were supplemented with SAM or allowed to recover for 48 h in complete

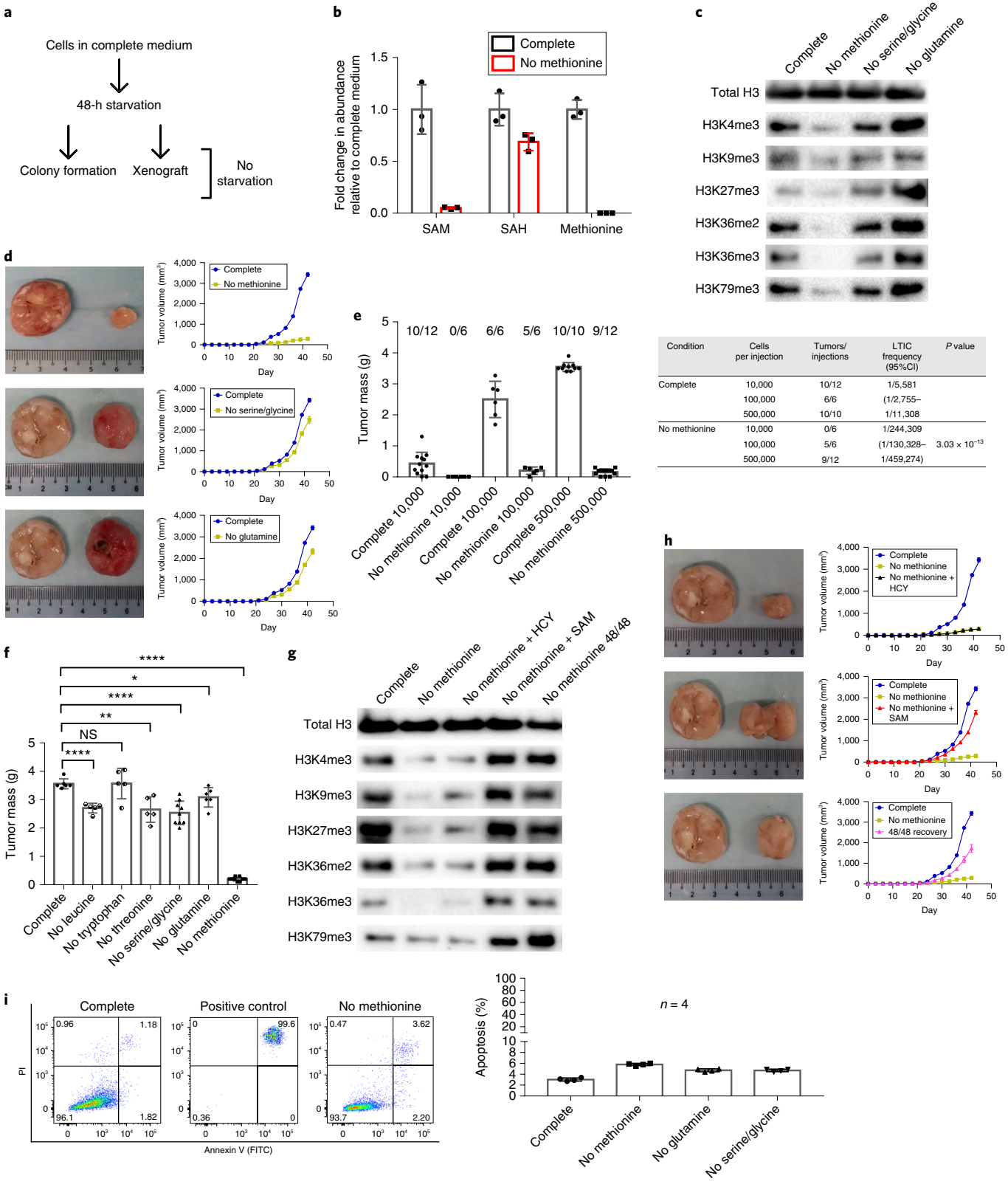

Condition	Cells per injection	Tumors/ injections	LTIC frequency (95%CI)	*P* value
Complete	10,000	10/12	1/5,581	
	100,000	6/6	(1/2,755–	
	500,000	10/10	1/11,308	
No methionine	10,000	0/6	1/244,309	
	100,000	5/6	(1/130,328–	3.03×10^{-13}
	500,000	9/12	1/459,274)	

medium, histone methylation was restored. Homocysteine supplementation, however, failed to rescue the effects of methionine starvation, indicating that tumorsphere cells require exogenous methionine for histone methylation (Fig. 2g). Colony- and tumor-forming capabilities under methionine starvation conditions were rescued when SAM was supplemented or when cells were allowed to recover for 48 h in complete medium (Fig. 2h and Extended Data Fig. 2f). Interestingly, the extent of rescue when cells were recovered for 48 h was not as dramatic as when the starvation medium was supplemented with SAM. This suggests that transient depletion of methionine can impact the tumorigenic capability of TICs, presumably by imposing long-term epigenetic alterations.

As a comparison, tumorsphere cells were starved of glutamine or both serine and glycine in the same manner. Short-term starvation for glutamine, which was highly abundant in tumorsphere cells, increased cellular histone methylation as a result of a decrease in the α-ketoglutarate/succinate ratio, whereas combined serine and glycine starvation had no impact on bulk histone methylation levels (Figs. 1h and 2c, and Extended Data Fig. 2g)[35]. Unexpectedly, these conditions only mildly hampered the ability to form colonies in soft agar and tumors in NSG mice, indicating that these amino acids are transiently dispensable for TIC function (Fig. 2d and Extended Data Fig. 2a). To exclude the possibility that transient amino acid starvation led to the loss of cell viability, we analyzed cells for apoptosis but did not find any large increase in the proportion of early apoptotic cells at 48 h (Fig. 2i). There was a slight increase (~2%) in the number of apoptotic cells starved for methionine, but the overall proportion remained low (Fig. 2i). Returning cells that were starved under these conditions to complete medium also led to recovery of proliferation, indicating that they remain viable after transient starvation (Extended Data Fig. 2h). In contrast to previous reports, methionine starvation did not lead to a block at the G2/M boundary (Extended Data Fig. 2i)[36,37].

We further tested whether the viability of cells was affected during the rescue conditions to ensure that we were not subjecting non-viable cells to downstream assays. In agreement with the tumorsphere cell starvation studies, the viability of cells under all three rescue conditions did not seem to be severely impacted (Extended Data Fig. 2j,k). Similarly to tumorsphere cells, adherent cells remained viable following transient methionine starvation (Extended Data Fig. 2k). These findings reinforce our observation that loss of tumor-forming capability in TICs is probably not the result of apoptosis or cell cycle arrest of viable cells, but is mediated directly through inhibition of methionine cycle activity.

Dependency on methionine cycle flux and SAM leads to addiction of tumor-initiating cells to methionine. The failure of exogenous homocysteine to rescue lung tumorsphere cells from methionine starvation could indicate that de novo synthesis of methionine was insufficient to meet the demands for methionine and SAM use. To trace the fate of methionine in TICs, we first performed short-term pulse–chase experiments with [^{13}C]methionine, followed by LC–MS detection and quantification (Extended Data Fig. 3a). Tumorsphere cells were initially starved of methionine for 16 h, followed by addition of [^{13}C]methionine and tracking of labeled metabolites (Extended Data Fig. 3b). Shortly after addition of labeled methionine, [^{13}C]methionine and derived metabolites were rapidly detected and reached steady state within 5 min (Extended Data Fig. 3b). Across multiple time points, the abundance of regenerated methionine and remethylated SAM remained comparatively low (Extended Data Fig. 3b). Because starvation before pulse–chase experiments may cause cellular stress and affect the steady state of methionine metabolism, we repeated the pulse–chase experiment under the complete nutrient condition and obtained results consistent with the previous observations (Extended Data Fig. 3b).

To further support the notion that lung TICs depend on exogenous methionine, we sought to investigate the basis for the inability of tumorsphere cells to use homocysteine. As a comparison, we included NIH 3T3 cells because they were able to use homocysteine and grow under methionine starvation conditions, despite lower relative abundance of all methionine cycle enzymes (Fig. 3a and Extended Data Fig. 3c). When using deuterium-labeled homocysteine, we found that the abundance of deuterated homocysteine and methionine in tumorsphere and NIH 3T3 cells was comparable at steady state, indicating comparable rates of homocysteine import and methionine regeneration (Fig. 3b,c). In contrast to NIH 3T3 cells, deuterated SAM was not detected in tumorsphere cells, suggesting that labeled-methionine-derived SAM was rapidly consumed in tumorsphere cells (Fig. 3c). This was supported by observations that deuterated SAH production and levels of methylated histones were higher in tumorsphere cells (Fig. 3c and Extended Data Fig. 3d). Hence, the data suggest that high SAM consumption rates in tumorsphere cells contribute to their dependency on exogenous methionine.

Fig. 3 | Metabolic labeling and tracking of methionine cycle flux. a, Methionine dependence in TICs and NIH 3T3 cells. Mean cell viability normalized and expressed as a percentage of starting mean viability at day 0 was assessed with CellTiter-Glo. Error bars, s.d.; $n=6$ biologically independent experiments. **b**, Schematic of deuterium-labeled homocysteine as it progresses through the methionine cycle. Deuterium atoms are denoted by pink stripes. **c**, Proportional abundance (% APE) of metabolite species, detected through labeled homocysteine pulse–chase experiments in TS32 and NIH 3T3 cells. Data represent the mean ± s.e.m.; $n=3$ technical replicate measurements. Technical replicates are shown to demonstrate the technical consistency of the method. Curves for two biological replicates are shown. **d**, Western blot analysis of *GLDC*-knockdown cells supplemented with SAM. SAM (500 μM) was added to *GLDC*-knockdown cells for 48 h, after which cells were collected. Histone H3 is used as a loading control. Independent blots were repeated at least three times with similar results. **e**, Mean volume of tumors seeded with 500,000 *GLDC*-knockdown cells grown under the indicated conditions before implantation. Error bars, s.e.m.; $n=4$ tumors. **f**, Western blot analysis of *GLDC*-knockdown cells supplemented with SAM. SAM (500 μM) was added to *GLDC*-knockdown cells for 48 h, after which cells were collected. GAPDH was used as a loading control. Independent blots were repeated at least three times with similar results. **g**, Proportional abundance (% APE) of metabolite species, detected through labeled homocysteine pulse–chase experiments in TS32 as well as *GLDC*-knockdown and *MTHFR*-knockdown cells. Data represent the mean ± s.e.m.; $n=3$ technical replicate measurements. Technical replicates are shown to demonstrate the technical consistency of the method. Curves for two biological replicates are shown. **h**, Top, mean volume of tumors seeded with 500,000 of the indicated tumorsphere-derived cell lines. Error bars, s.e.m.; $n=4$ tumors. Growth curves for control and *GDLC*-knockdown cells in Fig. 1c were included for comparison. Bottom, western blot analysis of the effect of MTHFR overexpression in *GLDC*-knockdown cell lines. GAPDH is used as a loading control for the MTHFR and GLDC immunoblots; total histone H3 is used as a loading control for the remaining blots. Independent blots were repeated at least three times with similar results. **i**, Schematic of the one-carbon pathway in relation to the methionine cycle. Metabolites used in the metabolite rescue experiments are indicated in blue. **j**, Levels of methylated histones in control-knockdown, *GLDC*-knockdown, and MTHFR-overexpressing + *GLDC*-knockdown cells with or without formate supplementation (0.5 mM). Histone H3 was used as a loading control. Independent blots were repeated at least three times with similar results. **k**, Levels of methylated histones in control-knockdown, *GLDC*-knockdown, and MTHFR-overexpressing + *GLDC*-knockdown cells with or without methyl-THF (20 μM) or adenosine (200 μM) supplementation. Histone H3 was used as a loading control. Independent blots were repeated at least three times with similar results. See also Extended Data Fig. 3.

Contribution of the one-carbon pathway to the methionine cycle. Because the methionine cycle lies downstream of the serine–glycine and one-carbon pathways, and methyl-THF units generated by MTHFR are used to regenerate methionine from homocysteine, we dissected the biochemical interactions between these metabolic pathways (Fig. 1f). We first evaluated the contributions of the methionine cycle in *GLDC*-knockdown cells by supplementing them with SAM to rescue cellular methylation before xenografting them into mice (Fig. 3d). This led to reestablishment of histone methylation, at least transiently, in *GLDC*-knockdown cells and incomplete rescue of tumorigenic potential (Fig. 3e and Extended Data Fig. 3e). We also observed recovery of MTHFR abundance in SAM-supplemented cells (Fig. 3f).

One-carbon flux supplies the MTHFR-generated methyl-THF units required for methionine remethylation. To understand the impact of GLDC and MTHFR downregulation on methionine cycle flux in TICs, we performed pulse–chase experiments with deuterium-labeled homocysteine in *GLDC*-knockdown and *MTHFR*-knockdown cells (Fig. 3g and Extended Data Fig. 3f). As expected, there was a dramatic decrease in the abundance of deuterated methionine in comparison to parental tumorsphere cells, despite similar rates of homocysteine import, indicating a defect in the

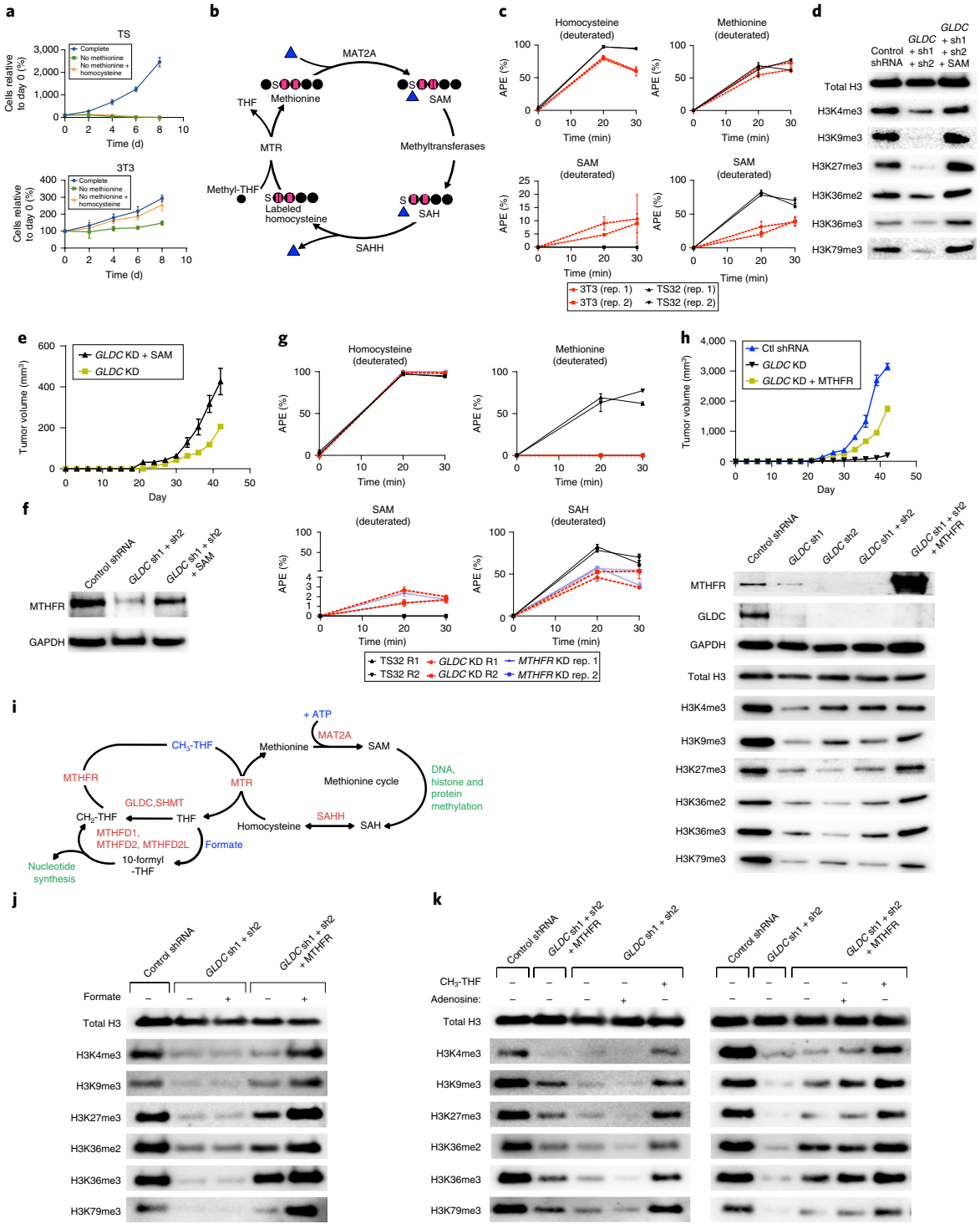

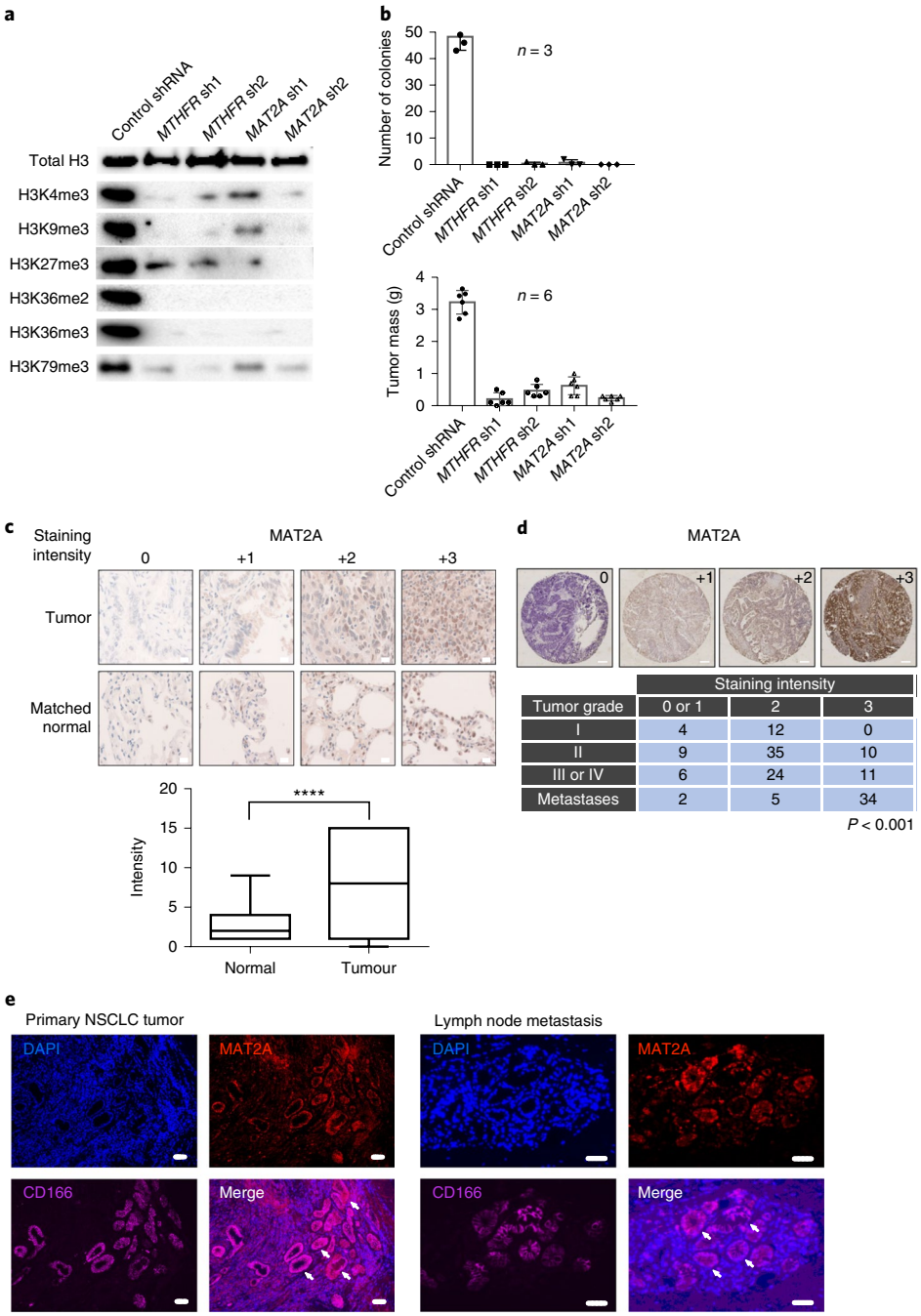

Fig. 4 | Functional and clinical relevance of methionine cycle enzymes in NSCLC. a, Western blot analysis of cell lines stably expressing shRNA against *MTHFR* or *MAT2A*. Total histone H3 is used as a loading control. Independent blots were repeated at least three times with similar results. **b**, Effect of *MTHFR* and *MAT2A* knockdown on the tumor-formation abilities of tumorsphere cells. Top, mean number of crystal-violet-stained colonies formed from knockdown cells; 5,000 cells were plated per well. Error bars, s.d.; $n = 3$ biologically independent experiments. Bottom, mean tumor mass in NSG mice following transplantation of 500,000 tumorsphere, *MTHFR*-knockdown or *MAT2A*-knockdown cells. Tumors were weighed 6 weeks after transplantation or when they reached 2 cm in diameter. Error bars, s.d.; $n = 6$ tumors for all injections. **c**, MAT2A immunohistochemistry was performed on 47 paired tumor and adjacent normal sections from different patients. Staining of the tumor microarray was performed once. Top, representative staining intensity. White bars, 20 μm. Bottom, box-and-whisker plots compare the staining intensity of tumor and normal sections. The box extends from the twenty-fifth to the seventy-fifth percentile, and whiskers denote minima and maxima. Intensity was defined as the product of the maximum immunostaining intensity and the percentage of tumor cells stained. The bold line within the box denotes median intensity; $^{****}P < 0.0001$, determined by paired Student's two-sided *t* test. $P < 0.0001$; $n = 47$ normal–tumor pairs, $t = 5.918$, d.f. = 46. **d**, MAT2A immunohistochemistry of an NSCLC tumor microarray ($n = 152$ different patients). Staining of the tumor microarray was performed once. Top, representative images and staining intensity grades (upper right corner). White bars, 200 μm. Bottom, a contingency table correlating the staining intensity of MAT2A with NSCLC grade. The chi-squared test *P* value is shown at the bottom right; $P < 0.0001$, $\chi^2 = 57.04$, d.f. = 6. **e**, Coimmunofluorescent staining of CD166 (pink) and MAT2A (red) on tumors from patients with lung cancer, counterstained with DAPI (blue). Representative images of primary NSCLC (left) and metastatic lymph node (right) tumors are shown. White arrows indicate representative cells where CD166 and MAT2A staining overlap. White bars, 40 μm. Imaging experiments were performed at least three times with similar results. See also Extended Data Fig. 4.

homocysteine remethylation step. *GLDC* and *MTHFR* knockdown both led to accumulation of deuterated SAH, thereby confirming that SAHH was driving the reverse reaction (backflux) owing to homocysteine accumulation[38]. Likewise, SAHH backflux was also observed in adherent cells (Extended Data Fig. 3g), which similarly exhibited defective homocysteine remethylation as a result of a decreased one-carbon pool, thereby possibly indicating reduced one-carbon flux (Fig. 1g and Extended Data Fig. 1e–g). This underscores the importance of methionine remethylation as a mechanism for clearing homocysteine from cells (Fig. 1g).

We speculated that reactivation of MTHFR could, to some extent, rescue the phenotype of *GLDC*-knockdown TICs (Fig. 1b–d). Overexpression of MTHFR in *GLDC*-knockdown cells only partially rescued histone methylation levels and tumorigenicity, as one-carbon flux probably remained crippled (Fig. 3h and Extended Data Fig. 3h). To understand the context in which one could elicit complete rescue of methylation activity, we performed metabolite supplementation in *GLDC*-knockdown or MTHFR-overexpressing + *GLDC*-knockdown cells (Fig. 3i–k). Supplementation with formate only fully rescued histone methylation in the latter cells, indicating that MTHFR and homocysteine remethylation are critical in maintaining methylation activity (Fig. 3j). Indeed, only direct supplementation with CH_3-THF to bypass the block at the MTHFR step led to rescue of histone methylation in *GLDC*-knockdown cells (Fig. 3k). Although one-carbon flux is also important in maintaining ATP pools, which serve as substrate for SAM synthesis, supplementation with formate or adenosine did not rescue histone methylation in *GLDC*-knockdown cells even though supplementation with both rescued ATP levels (Fig. 3j,k and Extended Data Figs. 1d and 3i)[28]. We reasoned that MTHFR and MAT2A could be potential therapeutic targets owing to SAM dependency. We knocked down *MAT2A* and *MTHFR* in tumorsphere cells, which led to a dramatic reduction in histone methylation, as well as impairments to soft agar colony- and tumor-forming capabilities, thus phenocopying the effects of methionine starvation and *GLDC* knockdown (Fig. 4a,b and Extended Data Fig. 4a). Together, these data indicate that the one-carbon pathway, acting through MTHFR and homocysteine remethylation, has a critical role in controlling the flux of methyl-THF units into the methionine cycle, thereby preventing accumulation of homocysteine.

To establish the clinical relevance of MAT2A and MTHFR expression in lung adenocarcinoma, we assessed their abundance in a panel of tumors derived from patients (Fig. 4c, Extended Data Fig. 4b and Supplementary Table 4). Both proteins were overexpressed in the majority of human lung tumors, but not in normal lung tissues. By using another tumor panel with tumor grading information, we found that MAT2A was strongly expressed in high-grade primary tumors or metastases, whereas such correlations were not seen with MTHFR expression (Fig. 4d, Extended Data Fig. 4c and Supplementary Table 4). Furthermore, CD166 was coexpressed with MAT2A in primary tumor cells. $CD166^+$ cells isolated from a human tumor also strongly expressed MAT2A, in contrast to the much lower expression observed in the corresponding counterparts found in normal lung tissues (Fig. 4e and Extended Data Fig. 4d). Knockdown of *MAT2A* had little or no effect on the proliferation of adherent or NIH 3T3 cells, underscoring its function in lung tumor-initiating tumorsphere cells (Extended Data Fig. 4e,f).

Small-molecule perturbation of the methionine cycle impacts the tumorigenicity of tumor-initiating cells. To evaluate the methionine cycle as a therapeutic target in lung TICs, we tested two inhibitors known to perturb methionine cycle activity and cellular methylation levels: (i) the MAT2A inhibitor FIDAS-5[39] and (ii) the SAHH inhibitor D9, which is an analog of DZNep (Fig. 5a)[40–42]. Inhibition by D9 led to accumulation of intracellular SAH (~30-fold increase relative to control cells). FIDAS-5 strongly reduced intracellular levels of SAM and SAH (~10-fold relative to control cells) and more potently inhibited methionine cycle activity than D9 in tumorsphere cells (Fig. 5b–d). Transient exposure of tumorsphere cells to D9 did not result in dramatic overall changes in histone methylation (Fig. 5d); however, unexpectedly, colony- and tumor-forming abilities were partially blocked (Fig. 5e and Extended Data

Fig. 5 | Small-molecule inhibition of the methionine cycle disrupts the tumorigenicity of lung tumor-initiating cells. a, Schematic of the methionine cycle and targets (in blue) of small-molecule inhibitors (in red) used in the study. **b**,**c**, Abundance of methionine cycle metabolites 48 h after treatment with D9 (**b**) or FIDAS-5 (**c**), as determined by LC–MS, normalized to abundance in DMSO-treated cells. Data represent the mean ± s.d.; $n = 3$ and 6 biologically independent experiments for D9 and FIDAS-5 treatment, respectively. **d**, Western blot analysis of cell lines treated with the specified inhibitors. Total histone H3 is used as a loading control. Independent blots were repeated at least three times with similar results. **e**,**f**, Effects of the D9 (**e**) and FIDAS-5 (**f**) inhibitors and methionine-cycle-related metabolites on the tumorigenic capabilities of lung cancer TICs. Top, mean number of crystal-violet-stained colonies formed from cells treated with inhibitor before the colony-forming assay; 5,000 cells were plated per well. Error bars, s.d.; $n = 8$ and 3 biologically independent experiments for the D9 and FIDAS-5 conditions, respectively. Bottom, mean volume of tumors seeded with 500,000 tumorsphere cells cultured under the specified conditions before implantation. Error bars, s.e.m.; $n = 4$ tumors. **g**, Intraperitoneal administration of compounds into mice subcutaneously implanted with 5×10^5 lung TICs. Mice were administered 40 mg per kg FIDAS-5, 4 mg per kg cisplatin or 100 µl of corn oil vehicle for 3 d following implantation. The mean volume of tumors seeded with 500,000 tumorsphere cells under the specified treatment regimens is shown. Error bars, s.e.m.; $n = 4$ tumors. **h**, Western blot analysis of MAT2A in a panel of cancer cell lines. GAPDH was used as a loading control. Independent blots were repeated at least three times with similar results. **i**, Proliferation of cancer cell lines grown in FIDAS-5-containing medium (10 µM final concentration). Cell lines are grouped according to whether FIDAS-5 inhibited (responsive) or did not inhibit (non-responsive) growth. Mean cell viability was normalized and is expressed as a percentage of the starting mean viability at day 0 was assessed with CellTiter-Glo. Error bars, s.d.; $n = 6$ biologically independent experiments. **j**, Top, intraperitoneal administration of FIDAS-5 (40 mg per kg) or corn oil vehicle into mice subcutaneously implanted with 5×10^5 lung PDX cells for 3 d. The identity of the PDX line is stated on the *x* axis. Tumors were collected and weighed 6 weeks after transplantation or when they reached 2 cm in diameter. Mean weights of tumors are indicated on the *y* axis. Error bars, s.d.; $n = 5$ tumors for A139 with corn oil injection; $n = 7$ tumors for A139 with FIDAS-5 injection; $n = 8$ tumors for both A233 conditions. Bottom, mean volume of PDX tumors in the indicated treatment regimes. Error bars, s.e.m.; $n = 4$ tumors. **k**,**l**, Analysis of human CD166 sorted cells from FIDAS-5-responsive PDXs. **k**, Protein levels of MAT2A and methylated histones in $CD166^+$ and $CD166^-$ sorted cells. GAPDH and total histone H3 were used as loading controls. Independent blots were repeated at least three times with similar results. **l**, Analysis of MAT2A and methylated histones in bulk PDX tumors following the indicated FIDAS-5 treatment regime. GAPDH and total histone H3 were used as loading controls. Independent blots were repeated at least three times with similar results. **m**, CD166 staining of vehicle- and FIDAS-5-treated tumors. Left, mean percentage of $CD166^+$ cells from the indicated PDX tumors and treatment conditions. Error bars, s.d.; $n = 3$ tumors. Right, representative flow cytometry plots of the indicated tumors and treatment conditions. Analysis was performed on three different tumors with similar results. **n**, Coimmunofluorescent staining of CD166 (cyan) and MAT2A (red) on PDXs, with DAPI counterstaining (blue). Representative images of PDXs treated with corn oil or FIDAS-5 are shown. Imaging experiments were performed at least three times with similar results. White arrows indicate representative cells where CD166 and MAT2A staining overlaps. White bars, 50 µm. See also Extended Data Fig. 5.

Fig. 5a). FIDAS-5 treatment resulted in complete ablation of all histone methylation marks analyzed in tumorsphere cells, with colony- and tumor-forming capabilities severely diminished, and a decrease in CD166 expression (Fig. 5d,f and Extended Data Fig. 5a,b). In contrast, NIH 3T3 and adherent cells, which are far less dependent on methionine, were unaffected, largely because there was no measurable turnover of methylated histones, over 8 h as compared to tumorsphere cells (Fig. 5d and Extended Data Fig. 5c). The high turnover of methylated histones in tumorsphere cells was rescued by treatment with the proteasomal inhibitor MG-132 or inhibition of a subset of histone demethylases by glutamine starvation, indicating that histone ubiquitination and demethylation are involved in destabilization of methylated histones in tumorsphere cells (Extended Data Fig. 5d).

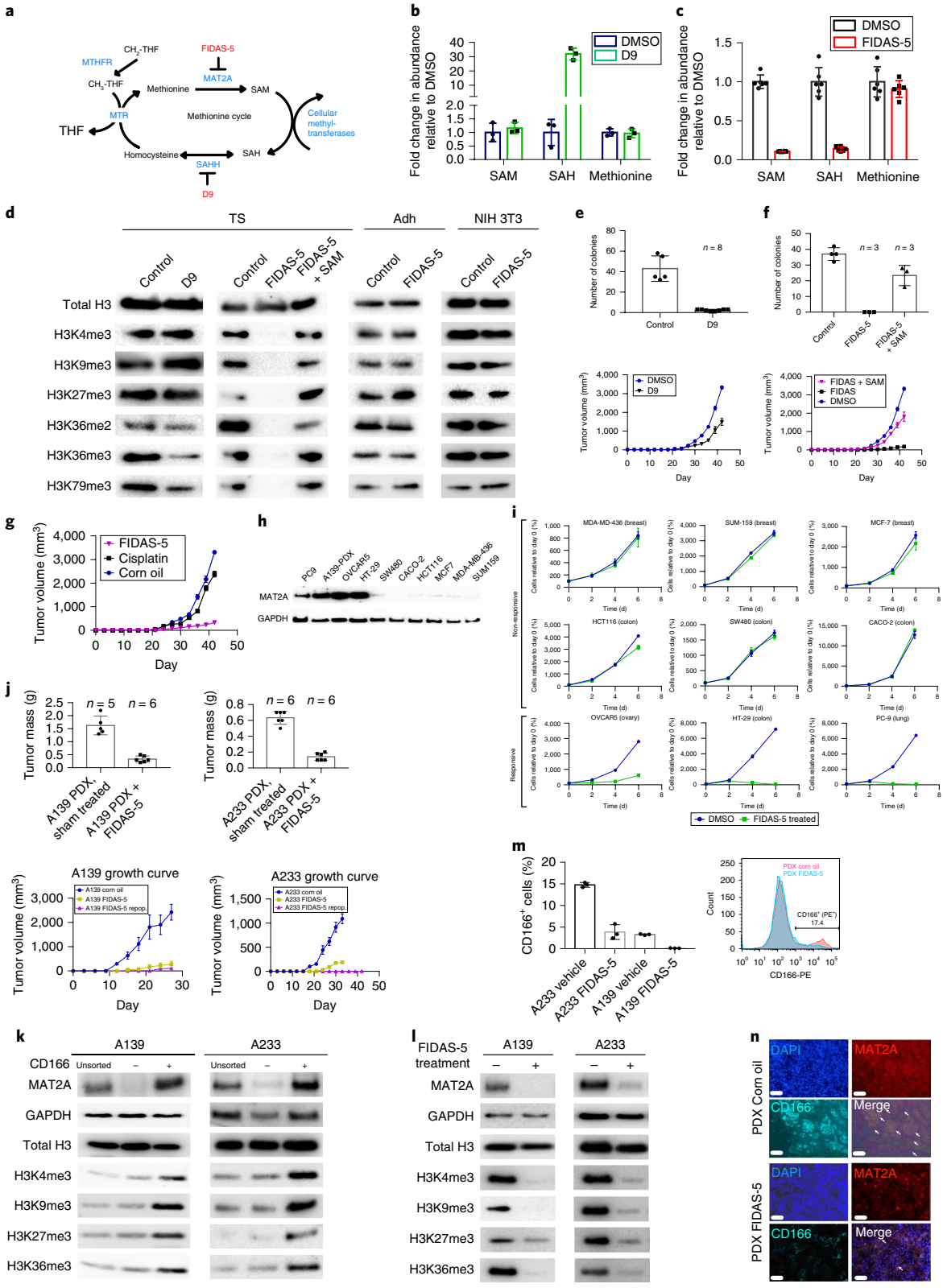

To exclude the possibility of general drug cytotoxicity, tumorsphere cells were transiently exposed to D9 or FIDAS-5, but to a large extent this did not negatively impact their long-term proliferation ability or trigger apoptosis (Extended Data Fig. 5e,f). Longer-term exposure to FIDAS-5 for 6 d before returning cells to medium without FIDAS-5, however, completely ablated their growth capacity, as expected (Extended Data Fig. 5g)[27]. Adherent and non-neoplastic cell lines were far less affected, thus highlighting the therapeutic potential of MAT2A inhibition (Extended Data Fig. 5h). We reasoned that addition of exogenous SAM could bypass MAT2A inhibition. Supplementation of tumorsphere cells with 500 µM SAM in the context of FIDAS-5 treatment to a large extent rescued histone methylation, as well as colony- and tumor-formation capabilities (Fig. 5d,f and Extended Data Fig. 5a).

Next, we sought to test whether FIDAS-5 could impact the tumorigenic potential of tumorsphere cells in animals. Tumorsphere cells were subcutaneously implanted into NSG mice and FIDAS-5 (40 mg per kg) or corn oil carrier was immediately administered via intraperitoneal injection for three consecutive days. After 6 weeks, FIDAS-5-treated mice had produced smaller tumors than carrier-treated controls (Fig. 5g and Extended Data Fig. 5i). Similarly, fewer pulmonary lesions were found in mice that were orthotopically implanted with tumorsphere cells and transiently treated with FIDAS-5 (Extended Data Fig. 5j). We compared the effects of FIDAS-5 treatment with those of cisplatin (4 mg per kg), a frontline chemotherapeutic agent in NSCLC tumors, in the same manner (Fig. 5g and Extended Data Fig. 5i). Cisplatin, however, was unable to halt tumor growth, strongly underscoring the resistance of TICs to chemotherapy. No loss in body weight was observed during the treatment period for either FIDAS-5- or control-treated mice (Extended Data Fig. 5k).

To understand the clinical relevance of MAT2A in cancer, we examined a collection of cancer cell lines with varying MAT2A expression across cancer types (Fig. 5h). The growth of cancer cells expressing high levels of MAT2A was hampered upon FIDAS-5 treatment, whereas cancer cells that expressed low levels of MAT2A were largely insensitive, thus implicating MAT2A and the methionine cycle in other cancers (Fig. 5i). To determine whether FIDAS-5 treatment could disrupt the growth of lung tumor patient-derived xenografts (PDXs), we treated NSG mice bearing two different PDX lines with FIDAS-5 (40 mg per kg) for 3 d immediately after implantation (Fig. 5j). We first verified that $CD166^+$ TICs sorted from these PDXs had elevated expression of MAT2A and higher abundance of methylated histones as compared to their $CD166^-$ non-TIC counterparts, suggesting sensitivity to MAT2A inhibition (Fig. 5k). Xenograft tumors that formed were at least fivefold smaller in FIDAS-5-treated mice than in vehicle-treated mice (Fig. 5j). Transient FIDAS-5 treatment led to strong downregulation of MAT2A expression and a decrease in the abundance of methylated histones in resultant residual tumors (Fig. 5l). In line with this, $CD166^+$ TICs were depleted and there was a decreased number of cells that coexpressed MAT2A and CD166 (Fig. 5m,n). To further demonstrate unequivocally that TICs were indeed largely ablated with FIDAS-5 treatment and that the residual tumors contained few TICs, we performed secondary transplantation and repopulation studies. Dissociated viable cells from FIDAS-5-treated tumors that were reimplanted into NSG mice were unable to form tumors (Fig. 5j). Taken together, these findings indicate that transient treatment with methionine cycle inhibitors, but not chemotherapy, may be sufficient to impact the growth of tumors that are driven by TICs and highlight the need to explore the use of metabolic enzyme inhibitors as a part of cancer treatment.

Discussion

An emerging hallmark of cancer is alteration of the cellular metabolism that supports cancer cell proliferation and tumor growth[43–45]. Dependence of neoplastic cells on exogenous methionine, which has thus far been largely overlooked, appears specific to transformed cells. Methionine dependency describes the scenario in which, under methionine starvation conditions, transformed cells are defective at using homocysteine as a methionine substitute for growth whereas untransformed fibroblasts are able to proliferate in homocysteine-supplemented medium[36,46–48]. In the context of tumor heterogeneity, cancer cell subpopulations may have different requirements for methionine, that is, heterogeneity in methionine metabolism that may impact their behavior[18,19]. Beyond influencing proliferation, increased methionine cycle flux is critical for driving tumorigenesis of TICs. Even short-term starvation for methionine, but not other amino acids, leads to dramatic disruption of tumor-initiating ability, which is largely attributable to blockade of cellular methylation in TICs. This underscores the less-appreciated influence of methionine cycle flux on epigenetic programs that are associated with tumor initiation or cancer progression. Nevertheless, we note that experimental isolation of TICs or the use of surface markers may not faithfully reflect the behavior of TICs in intact tumors[49]. Indeed, across human lung tumors, variations were observed in the expression of enzymes controlling methionine metabolism, and this altered expression was correlated with TIC markers (Fig. 4c–e). While use of different cell culture conditions has enabled us to delineate cells by tumor-initiating properties in vitro and ex vivo, the plasticity of TICs and the contribution of the tumor microenvironment to TIC function and methionine metabolism need further investigation[19,50–52].

Prolonged methionine starvation in immunocompromised mice could reduce tumor load but was eventually lethal[53]. We found here that transient methionine depletion could produce long-term disruption of TIC function, and we highlight methionine cycle inhibition as a TIC-targeting strategy. More broadly, MAT2A expression was significantly higher in other cancers we examined than in their corresponding normal tissues (Extended Data Fig. 5l). Furthermore, elevated expression of MAT2A (but not MTHFR) in high-grade lung tumors and metastases indicates the higher dependency on methionine cycle activity and SAM production of these tumor cells and could mark them for targeted therapies. Interestingly, MAT2A was observed to be nuclear (Figs. 4e and 5n), in line with previous reports that it can associate with chromatin[54–56]. Nuclear localization of MAT2A could allow SAM to be immediately synthesized and consumed by methyltransferases, thereby contributing to high SAM consumption and kinetics of methylated histone turnover (Fig. 3c and Extended Data Fig. 5c).

It was recently shown that targeting MAT2A flux in *MTAP*-null cancer lines could be a means to attenuate the oncogenic activity of PRMT5[57]. We note, however, that our TIC lines express MTAP and have comparable levels of symmetric dimethylarginine, similar to the reference HCT116 cells wild type for MTAP used in that study (Extended Data Fig. 5m). Thus, in our study, the dependency on methionine as a therapeutic vulnerability does not appear to be dependent on the MTAP–MAT2A–PRMT5 axis.

A remaining question is the mechanism through which global inhibition of histone methylation has a distinct effect on the tumorigenicity of TICs but not the proliferation of non-TICs. The precise mechanism by which methylated histones control gene expression patterns at the genome scale is unclear, although one study demonstrated that bulk histone but not DNA methylation was crucial for driving epithelial–mesenchymal transition in cancer cells[58]. This suggests that, despite the potentially widespread impact of methionine cycle inhibition, only a subset of methylation events might be critical for TIC tumorigenic properties. Conversely, histone methylation is globally downregulated in non-TICs; the nature of key genomic loci regulating the differentiated cell state requires further elucidation. Quite possibly, the p53–p38 stress signaling pathway may have a role in response to methionine cycle inhibition in TICs;

this pathway has been shown to be critical in the differentiation of embryonic stem cells in response to methionine deprivation[25,26]. Subsequent efforts should focus on uncovering the suite of stress-induced and downstream transcriptional and proteomic targets. Our findings demonstrate that functional subpopulations of carcinoma cells within a tumor have different metabolic dependencies and highlight the need to understand cellular metabolism in the context of tumor heterogeneity[59,60].

Online content

Any methods, additional references, Nature Research reporting summaries, source data, statements of code and data availability and associated accession codes are available at https://doi.org/10.1038/s41591-019-0423-5.

Received: 21 December 2016; Accepted: 14 March 2019;
Published online: 6 May 2019

References

1. Chaneton, B. et al. Serine is a natural ligand and allosteric activator of pyruvate kinase M2. *Nature* **491**, 458–462 (2012).
2. DeBerardinis, R. J., Lum, J. J., Hatzivassiliou, G. & Thompson, C. B. The biology of cancer: metabolic reprogramming fuels cell growth and proliferation. *Cell Metab.* **7**, 11–20 (2008).
3. Jain, M. et al. Metabolite profiling identifies a key role for glycine in rapid cancer cell proliferation. *Science* **336**, 1040–1044 (2012).
4. Maddocks, O. D. et al. Serine starvation induces stress and p53-dependent metabolic remodelling in cancer cells. *Nature* **493**, 542–546 (2013).
5. Mayers, J. R. & Vander Heiden, M. G. Famine versus feast: understanding the metabolism of tumors in vivo. *Trends Biochem. Sci.* **40**, 130–140 (2015).
6. Vander Heiden, M. G. et al. Metabolic pathway alterations that support cell proliferation. *Cold Spring Harb. Symp. Quant. Biol.* **76**, 325–334 (2011).
7. Wise, D. R. & Thompson, C. B. Glutamine addiction: a new therapeutic target in cancer. *Trends Biochem. Sci.* **35**, 427–433 (2010).
8. Anastasiou, D. et al. Inhibition of pyruvate kinase M2 by reactive oxygen species contributes to cellular antioxidant responses. *Science* **334**, 1278–1283 (2011).
9. Kim, D. et al. SHMT2 drives glioma cell survival in ischaemia but imposes a dependence on glycine clearance. *Nature* **520**, 363–367 (2015).
10. Son, J. et al. Glutamine supports pancreatic cancer growth through a KRAS-regulated metabolic pathway. *Nature* **496**, 101–105 (2013).
11. Locasale, J. W. et al. Phosphoglycerate dehydrogenase diverts glycolytic flux and contributes to oncogenesis. *Nat. Genet.* **43**, 869–874 (2011).
12. Possemato, R. et al. Functional genomics reveal that the serine synthesis pathway is essential in breast cancer. *Nature* **476**, 346–350 (2011).
13. Kaelin, W. G. Jr & McKnight, S. L. Influence of metabolism on epigenetics and disease. *Cell* **153**, 56–69 (2013).
14. Kaelin, W. G. Jr Cancer and altered metabolism: potential importance of hypoxia-inducible factor and 2-oxoglutarate-dependent dioxygenases. *Cold Spring Harb. Symp. Quant. Biol.* **76**, 335–345 (2011).
15. Lu, C. et al. *IDH* mutation impairs histone demethylation and results in a block to cell differentiation. *Nature* **483**, 474–478 (2012).
16. Letouze, E. et al. *SDH* mutations establish a hypermethylator phenotype in paraganglioma. *Cancer Cell* **23**, 739–752 (2013).
17. Xiao, M. et al. Inhibition of α-KG-dependent histone and DNA demethylases by fumarate and succinate that are accumulated in mutations of FH and SDH tumor suppressors. *Genes Dev.* **26**, 1326–1338 (2012).
18. Kreso, A. & Dick, J. E. Evolution of the cancer stem cell model. *Cell Stem Cell* **14**, 275–291 (2014).
19. Meacham, C. E. & Morrison, S. J. Tumour heterogeneity and cancer cell plasticity. *Nature* **501**, 328–337 (2013).
20. O'Brien, C. A., Kreso, A. & Dick, J. E. Cancer stem cells in solid tumors: an overview. *Semin. Radiat. Oncol.* **19**, 71–77 (2009).
21. Oskarsson, T., Batlle, E. & Massague, J. Metastatic stem cells: sources, niches, and vital pathways. *Cell Stem Cell* **14**, 306–321 (2014).
22. Tan, W. L. et al. Novel therapeutic targets on the horizon for lung cancer. *Lancet Oncol.* **17**, e347–e362 (2016).
23. Lee, Y. A. et al. Identification of tumor initiating cells with a small-molecule fluorescent probe by using vimentin as a biomarker. *Angew. Chem. Int. Ed. Engl.* **57**, 2851–2854 (2018).
24. Zhang, W. C. et al. Glycine decarboxylase activity drives non-small cell lung cancer tumor-initiating cells and tumorigenesis. *Cell* **148**, 259–272 (2012).
25. Shiraki, N. et al. Methionine metabolism regulates maintenance and differentiation of human pluripotent stem cells. *Cell Metab.* **19**, 780–794 (2014).
26. Tsuyama, T., Shiraki, N. & Kume, S. Definitive endoderm differentiation of human embryonic stem cells combined with selective elimination of undifferentiated cells by methionine deprivation. *Methods Mol. Biol.* **1341**, 173–180 (2016).
27. Shyh-Chang, N. et al. Influence of threonine metabolism on *S*-adenosylmethionine and histone methylation. *Science* **339**, 222–226 (2013).
28. Maddocks, O. D., Labuschagne, C. F., Adams, P. D. & Vousden, K. H. Serine metabolism supports the methionine cycle and DNA/RNA methylation through de novo ATP synthesis in cancer cells. *Mol. Cell* **61**, 210–221 (2016).
29. Labuschagne, C. F., van den Broek, N. J., Mackay, G. M., Vousden, K. H. & Maddocks, O. D. Serine, but not glycine, supports one-carbon metabolism and proliferation of cancer cells. *Cell Rep.* **7**, 1248–1258 (2014).
30. Martinez-Chantar, M. L. et al. L-Methionine availability regulates expression of the methionine adenosyltransferase 2A gene in human hepatocarcinoma cells: role of *S*-adenosylmethionine. *J. Biol. Chem.* **278**, 19885–19890 (2003).
31. Pendleton, K. E. et al. The U6 snRNA m6A methyltransferase METTL16 regulates SAM synthetase intron retention. *Cell* **169**, 824–835 (2017).
32. Quinlan, C. L. et al. Targeting *S*-adenosylmethionine biosynthesis with a novel allosteric inhibitor of Mat2A. *Nat. Chem. Biol.* **13**, 785–792 (2017).
33. Eagle, H. The specific amino acid requirements of a human carcinoma cell (Stain HeLa) in tissue culture. *J. Exp. Med.* **102**, 37–48 (1955).
34. Eagle, H., Oyama, V. I. & Levy, M. Amino acid requirements of normal and malignant human cells in tissue culture. *Arch. Biochem. Biophys.* **67**, 432–446 (1957).
35. Carey, B. W., Finley, L. W. S., Cross, J. R., Allis, C. D. & Thompson, C. B. Intracellular α-ketoglutarate maintains the pluripotency of embryonic stem cells. *Nature* **518**, 413–416 (2015).
36. Guo, H. Y., Herrera, H., Groce, A. & Hoffman, R. M. Expression of the biochemical defect of methionine dependence in fresh patient tumors in primary histoculture. *Cancer Res.* **53**, 2479–2483 (1993).
37. Yano, S. et al. Selective methioninase-induced trap of cancer cells in S/G2 phase visualized by FUCCI imaging confers chemosensitivity. *Oncotarget* **5**, 8729–8736 (2014).
38. De La Haba, G. & Cantoni, G. L. The enzymatic synthesis of *S*-adenosyl-L-homocysteine from adenosine and homocysteine. *J. Biol. Chem.* **234**, 603–608 (1959).
39. Zhang, W. et al. Fluorinated *N*,*N*-dialkylaminostilbenes repress colon cancer by targeting methionine *S*-adenosyltransferase 2A. *ACS Chem. Biol.* **8**, 796–803 (2013).
40. Jiang, X. et al. Functional characterization of D9, a novel deazaneplanocin A (DZNep) analog, in targeting acute myeloid leukemia (AML). *PloS One* **10**, e0122983 (2015).
41. Miranda, T. B. et al. DZNep is a global histone methylation inhibitor that reactivates developmental genes not silenced by DNA methylation. *Mol. Cancer Ther.* **8**, 1579–1588 (2009).
42. Tan, J. et al. Pharmacologic disruption of Polycomb-repressive complex 2-mediated gene repression selectively induces apoptosis in cancer cells. *Genes Dev.* **21**, 1050–1063 (2007).
43. Cantor, J. R. & Sabatini, D. M. Cancer cell metabolism: one hallmark, many faces. *Cancer Discov.* **2**, 881–898 (2012).
44. Hanahan, D. & Weinberg, R. A. Hallmarks of cancer: the next generation. *Cell* **144**, 646–674 (2011).
45. Ward, P. S. & Thompson, C. B. Metabolic reprogramming: a cancer hallmark even Warburg did not anticipate. *Cancer Cell* **21**, 297–308 (2012).
46. Halpern, B. C., Clark, B. R., Hardy, D. N., Halpern, R. M. & Smith, R. A. The effect of replacement of methionine by homocystine on survival of malignant and normal adult mammalian cells in culture. *Proc. Natl Acad. Sci. USA* **71**, 1133–1136 (1974).
47. Hoffman, R. M. & Erbe, R. W. High in vivo rates of methionine biosynthesis in transformed human and malignant rat cells auxotrophic for methionine. *Proc. Natl Acad. Sci. USA* **73**, 1523–1527 (1976).
48. Stern, P. H., Wallace, C. D. & Hoffman, R. M. Altered methionine metabolism occurs in all members of a set of diverse human tumor cell lines. *J. Cell. Physiol.* **119**, 29–34 (1984).
49. Batlle, E. & Clevers, H. Cancer stem cells revisited. *Nat. Med.* **23**, 1124–1134 (2017).
50. Lyssiotis, C. A. & Kimmelman, A. C. Metabolic interactions in the tumor microenvironment. *Trends Cell Biol.* **27**, 863–875 (2017).
51. Mayers, J. R. et al. Tissue of origin dictates branched-chain amino acid metabolism in mutant *Kras*-driven cancers. *Science* **353**, 1161–1165 (2016).
52. Davidson, S. M. et al. Environment impacts the metabolic dependencies of Ras-driven non-small cell lung cancer. *Cell Metab.* **23**, 517–528 (2016).
53. Guo, H. et al. Therapeutic tumor-specific cell cycle block induced by methionine starvation in vivo. *Cancer Res.* **53**, 5676–5679 (1993).
54. Ikeda, S., Kawahara-Miki, R., Iwata, H., Sugimoto, M. & Kume, S. Role of methionine adenosyltransferase 2A in bovine preimplantation development and its associated genomic regions. *Sci. Rep.* **7**, 3800 (2017).
55. Katoh, Y. et al. Methionine adenosyltransferase II serves as a transcriptional corepressor of Maf oncoprotein. *Mol. Cell* **41**, 554–566 (2011).

56. Kera, Y. et al. Methionine adenosyltransferase II-dependent histone H3K9 methylation at the *COX-2* gene locus. *J. Biol. Chem.* **288**, 13592–13601 (2013).
57. Marjon, K. et al. MTAP deletions in cancer create vulnerability to targeting of the MAT2A/PRMT5/RIOK1 axis. *Cell Rep.* **15**, 574–587 (2016).
58. McDonald, O. G., Wu, H., Timp, W., Doi, A. & Feinberg, A. P. Genome-scale epigenetic reprogramming during epithelial-to-mesenchymal transition. *Nat. Struct. Mol. Biol.* **18**, 867–874 (2011).
59. Feinberg, A. P., Ohlsson, R. & Henikoff, S. The epigenetic progenitor origin of human cancer. *Nat. Rev. Genet.* **7**, 21–33 (2006).
60. Hansen, K. D. et al. Increased methylation variation in epigenetic domains across cancer types. *Nat. Genet.* **43**, 768–775 (2011).

Acknowledgements

We thank SingHealth Advanced Molecular Pathology Laboratory for their assistance in generating tumor microarray data, M.Y. Lee, K.H.E. Lim, X.H. Yeo, G.S. Tan, M. Nichane, L. Chen, W.A. Zaw, S.L. Khaw, M.S. Noghabi and R. Ettikan for technical assistance, and S.-C. Ng for critical comments. This research is supported by the National Research Foundation, Singapore (NRF-NRFF2015-04), the National Medical Research Council, Singapore (LCG17MAY004; NMRC/OFIRG/0064/2017; NMRC/TCR/007-NCC/2013; OFYIRG16nov013), the Agency for Science, Research and Technology, Singapore (1331AEG071; 334I00053; SPF 2012/001), and the Singapore Ministry of Education under its Research Centers of Excellence initiative. Z. Wang dedicates this manuscript to the memory of Joseph P. Calarco, a wonderful friend and scientist.

Author contributions

L.Y.Y., P.K.W.C., C.C.T., K.L.E.P., N.B. and Y.S.H. performed metabolomic studies. Z. Wang, J.H.J.L., H.Y.-K.A., L.S.K.C., H.Y.C., X.J. and Z. Wu performed molecular, cell-based and mouse xenograft experiments. A.T., A.M.H., Q.Y., E.H.T., W.T.L., T.K.H.L., J.Y., S.M. and D.S.W.T. provided key reagents and interpreted the data. Z. Wang, B.L. and W.L.T. designed the research and wrote the manuscript.

Competing interests

The authors declare no competing interests.

Additional information

Extended data is available for this paper at https://doi.org/10.1038/s41591-019-0423-5.

Supplementary information is available for this paper at https://doi.org/10.1038/s41591-019-0423-5.

Reprints and permissions information is available at www.nature.com/reprints.

Correspondence and requests for materials should be addressed to B.L. or W.L.T.

Methods

Tissue culture. Two tumorsphere lines independently derived from two patients and tumorsphere *GLDC*-knockdown lines were maintained in DMEM/F12 (US Biomedical) supplemented with 4 mg ml^{-1} BSA (Sigma), non-essential amino acids, sodium pyruvate (Life Technologies), 20 ng ml^{-1} epidermal growth factor (EGF), 4 ng ml^{-1} basic fibroblast growth factor (bFGF) and insulin–transferrin selenium (ITS; Sigma). Tumorsphere-derived adherent cells and NIH 3T3 lines were maintained in the same medium without EGF, bFGF, ITS and BSA and were instead supplemented with 10% FBS. Glutamine, methionine, serine/glycine, leucine, tryptophan and threonine starvation media were generated from DMEM/F12 powder (US Biomedical) lacking the corresponding metabolites. Sodium formate and 5-methyl-THF disodium salt were purchased from Santa Cruz Biotechnology.

Inhibitors. Cisplatinum (*cis*-diammineplatinum(II) dichloride) and MG-132 (10 μM final concentration) were purchased from Sigma, FIDAS-5 (final concentration of 10 μM in culture medium) was from Merck Millipore.

Immunohistochemistry analyses. The NSCLC tumor microarray ($n = 47$) comprising paired formalin-fixed, paraffin-embedded normal and tumor samples from patients at 4-μm thickness was constructed and immunohistochemistry was performed by the SingHealth Advanced Molecular Pathology Laboratory at Singapore General Hospital by using a Bond Leica Machine with Bond Epitope solution 1. The staged tissue tumor microarray (LUM961and LUC1021) comprising formalin-fixed, paraffin-embedded primary and metastatic NSCLC tumors was purchased from Pantomics. Anti-MTHFR (ab125707) from Abcam and anti-MAT2A (HPA043028) from Sigma were used for both immunohistochemistry analyses. Immunohistochemistry for the staged tissue microarray sections was performed with VECTASTAIN ABC kits (Vector Labs). Samples were subsequently scored by visual assessment as '0 or +1', '+2' or '+3', according to staining intensity for MAT2A and MTHFR.

Flow cytometry and FACS. Cells were stained with antibodies conjugated with PE against human CD166 (R&D Systems, FAB6561P)[24] in DPBS containing 5% FBS for 1 h at 4 °C. Cells were then washed and resuspended in DPBS. The fluorescence intensity was measured on a flow cytometer (BD LSR II). Cell sorting was performed on a FACSAria II (BD). See Supplementary Fig. 1 for a representative gating strategy.

Immunofluorescence analyses. Formalin-fixed, paraffin-embedded NSCLC samples were obtained and cut into 4-μm sections. Sections were deparaffinized and antigen retrieval was carried out in citrate buffer in the presence of 0.5% Tween-20. Sections were further permeabilized in 0.2% Triton X-100 and then quenched with TruBlack (Gold Biotechnology). Sections were then incubated with anti-MAT2A (GTX50027)[39] from Genetex and anti-CD166 (HPA010926)[61] from Sigma. Alexa Fluor 594 donkey anti-mouse (A21203) and Alexa Fluor 647 goat anti-rabbit (A21245) antibodies from Thermo Fisher were used as secondary antibodies. Images were visualized and captured with a Zeiss Observer D1 epifluorescence microscope.

Tumor implantation and collection. 5×10^5 single cells were mixed in a 1:1 mixture of serum-free DMEM/F12 and Matrigel (BD) and injected subcutaneously into the flanks of 4- to 6-week-old male and female NSG mice (Jackson Laboratories). About 6 weeks later, or when tumor sizes exceeded 2 cm in diameter, mice were killed and tumors were collected for analysis. All mouse experiments were approved by the Agency for Science, Technology and Research of Singapore–Biological Resource Centre IACUC (protocol number 171286). We have complied with relevant ethical regulations pertaining to the IACUC protocol. The use of PDXs has been approved by the SingHealth Centralised Institutional Review Board (CIRB reference number 2007/444/B). We have complied with relevant ethical regulations pertaining to the IRB. Written informed consent was obtained from all participating patients diagnosed with non-small-cell adenocarcinoma before surgical resection or biopsy. All PDX tumors were maintained by passaging into new NSG recipient mice without cell culture. PDX tumors were dissociated and injected as previously described[24]. Briefly, tumors were collected in cold PBS with antibiotics, chopped with a sterile blade and incubated in 1 mg ml^{-1} collagenase/dispase (Sigma-Aldrich) in DMEM/F12 medium (Thermo Fisher Scientific) at 37 °C with agitation. Suspensions were then washed in PBS and passed through 70- and 40-μm cell strainers, centrifuged and evaluated for cell viability by tryphan blue exclusion before downstream assays. Mice were randomized by sex.

Tumor volume measurements. Tumor volume was calculated by the formula $0.5 \times l \times w^2$, where l and w are tumor length and width, respectively.

Orthotopic tumor implantation. 1.5×10^6 single tumorsphere cells expressing GFP (transduced with PLL3.7 vector) were suspended in tumorsphere medium and injected intravenously into the tail vein of 4- to 6-week-old male and female NSG mice (Jackson Laboratories). Mice were continuously monitored and then killed at 5 weeks after injection. Lungs were collected, fixed in 4% paraformaldehyde and embedded in paraffin for subsequent analysis. Anti-GFP (ab13970)[62] antibody from Abcam and Alexa Fluor 488 goat anti-chicken (A-11039) antibody from Thermo Fisher were used to visualize and quantify GFP-positive lesions via the immunofluorescence protocol outlined above. Mice were randomized by sex.

Cell proliferation assays. Cells were seeded into 96-well plates at a density of 2,000 cells per well for tumorsphere cells and 500 cells per well for adherent cells. Mean cell viability normalized and expressed as a percentage of the starting mean viability at day 0 was assessed every 2 d with CellTiter-Glo luminescence reagent (Promega).

ATP analyses. Cells were seeded into 96-well plates at a density of 1,000 cells per well in ten replicate wells per condition. Cells were then left to equilibrate at 37 °C for 3 h. ATP was quantified with CellTiter-Glo reagent (Promega). Five biological replicates were used.

Soft agar colony formation. 2.5 ml of a lower layer consisting of 0.7% agar in complete DMEM/F12 medium with 10% FBS was placed in three wells of a six-well dish and permitted to solidify. 5,000 cells per well were then suspended in a 2-ml layer of 0.35% agar in complete DMEM/F12 medium with 10% FBS and layered on top of the bottom layer. Colonies were stained with crystal violet and counted after approximately 2 months.

Apoptosis assays. 1×10^6 cells were stained with FITC Annexin V and PI from an apoptosis detection kit (BD, 556547) and analyzed for apoptosis by flow cytometry on an LSR II Cell Analyzer (BD) according to the manufacturer's recommendations.

Cell cycle analysis. Cell cycle analysis was performed by using the BD Pharmingen BrdU FITC Flow kit (559619) according to the manufacturer's recommendations.

ECAR measurement. ECAR measurement was performed by using an XF96 Extracellular Flux analyzer (Seahorse Bioscience) as described[63]. Briefly, adherent cells were plated into XF96 (V3) polystyrene cell culture plates at a cell density of 40,000 cells per well 1 d before the assay. Tumorsphere cells were then plated into XF96 (V3) polystyrene cell culture plates coated with Corning Cell-Tak Cell and Tissue Adhesive at a cell density of 50,000 cells per well on the day of the assay. Both cell lines were incubated for 24 h in a humidified 37 °C incubator with 5% CO_2 before the assay. While sensor cartridges were calibrated, cell plates were incubated in a 37 °C non-CO_2 incubator for 60 min before the start of an assay with appropriate assay medium at 175 μl per well. 25 μl of compound was added to each injection port. All experiments were performed at 37 °C. ECAR data points refer to individual rates measured from each well during the measurement cycles and are reported as absolute rates (mpH min^{-1}). ECAR values were then normalized to cell number with DAPI staining read at 340 nm.

Metabolomic analyses. The following reagents and materials were purchased from the indicated sources: Optima-grade methanol, Fisher Scientific; deionized water (18.2 mΩ), Sartorius; tricine salt and sodium chloride, Sigma-Aldrich; acetonitrile, chloroform and formic acid, Merck; isotope-labeled [$^{13}C_5$,^{15}N]methionine, Sigma; [$^2D_4$]homocysteine, Cambridge Isotope Laboratories.

Sample preparation of cell lysate for metabolomic analyses. For suspension cell culture, 10 million cells per sample were obtained and quenched with 4 volumes of ice-cold 150 mM sodium chloride solution. Cell pellets were collected by centrifugation of the quenched samples at 3,000*g* for 5 min at 4 °C and the supernatant was aspirated and discarded. For adherent cell culture, the medium was gently aspirated and cells on the surface of the well plates were gently washed three times with ice-cold 150 mM sodium chloride solution. Ice-cold sodium chloride solution was added to the plate and a cell scraper was used to release adherent cells from the plate surface. Cell pellets were collected as described above and kept on ice. For pulse–chase analysis, cells that were starved of methionine for 16 h in methionine-free medium were given a single treatment of [$^{13}C_5$,^{15}N] methionine or [$^2D_4$]homocysteine. Cells were either lysed immediately as described above or a chase was performed in incubation medium for various times.

Cell pellets were extracted by using a two-phase liquid–liquid extraction protocol based on the modified method of Bligh and Dyer[64]. Briefly, methanol, chloroform and 3.8 mM tricine solution (approximately 1:1:0.5 vol/vol) was used to separate polar metabolites (aqueous fraction) from lipid species (organic fraction). Polar metabolites in the aqueous fraction comprising methanol and water were collected in 2-ml Eppendorf tubes. Extracts were stored at −80 °C before UPLC–MS analysis. Samples were dried under vacuum pressure at 4 °C with a CentriVap centrifugal vacuum concentrator (Labconco) and reconstituted in 5% methanol–water solution before LC–MS analysis.

UPLC–MS analysis. Untargeted LC–MS analysis of polar metabolites was performed by using a UPLC system (ACQUITY, Waters Corp) interfaced with a mass spectrometer (LTQ-Orbitrap, Thermo Scientific). Electrospray ionization (ESI) in the mass spectrometer was conducted in both positive and negative mode

in full scan with a mass range of 50 to 1,000 m/z at a resolution of 15,000. Sheath and auxiliary gas flow were set at 40 and 15 (arbitrary units), respectively, with a capillary temperature of 400 °C. The ESI source and capillary voltages were 4.5 kV and 40 V, respectively, for positive ESI mode and 2.8 kV and −15 V for negative ESI mode. Mass calibration was performed with standard LTQ-Orbitrap calibration solution (Thermo Scientific) before sample injection. A pooled quality-control mixture comprising equal aliquots of all samples was run at regular intervals throughout each analytical batch. Samples were randomized for each analytical batch and triplicate injections were performed for each sample.

Targeted LC–MS/MS analysis was performed on a UPLC system (ACQUITY, Waters Corp) interfaced to a triple-quadrupole mass spectrometer (Xevo TQ-S, Waters Corp). Multiple-reaction monitoring (MRM) experiments were performed in both ESI positive and ESI negative mode with an elution gradient as described in Supplementary Table 5. Compound-dependent MS parameters for the analytes are shown in Supplementary Table 6. The source temperature and desolvation temperature were set at 150 °C and 500 °C, respectively. The cone gas flow was 150 liters h^{-1} and the desolvation gas flows were 700 liters h^{-1} (ESI positive mode) and 300 liters h^{-1} (ESI negative mode). The capillary voltage was 2.90 kV for positive ESI mode and 1.0 kV for negative ESI mode.

MRM transitions and MS parameters were optimized by using either analytical-grade standards or intracellularly synthesized metabolites (labelled as '*' in Supplementary Tables 6 and 7).

All chromatographic separations were performed on an ACQUITY UPLC HSS T3 1.7 µm, 50 × 2.1 mm i.d. column (Waters Corp). The column and autosampler temperatures were maintained at 30 °C and 4 °C, respectively. The elution condition is indicated in Supplementary Table 5. The injection volume was 4 µl.

Data preprocessing and metabolite identification. For untargeted LC–MS, raw UPLC–MS data were preprocessed and analyzed with the XCMS peak-finding algorithm (version 1.30.3)[65]. The pooled quality-control mixture was used for signal correction between and within each batch analysis. Samples were normalized on the basis of their cell counts. The identities of marker metabolites were verified by comparison of their retention time and mass spectra with those of commercially available standards.

For targeted LC–MS analysis, chromatographic peak integration was performed with Targetlynx software (version 4.1 SCN810, Waters Corp). In addition, for [^{13}C]methionine pulse–chase experiments, the APE for each species was calculated and natural abundance was corrected for by using an isotopomer matrix accounting for the presence of natural abundance carbons distributed throughout each possible precursor–fragment ion combination (Supplementary Table 7)[66].

RNA interference and lentiviral transduction. shRNAs were cloned into the pLKO.1 lentiviral plasmid (Addgene). Two shRNAs each were used against *GLDC*, *MAT2A* and *MTHFR*. Tumorsphere lines were infected with plKO.1 lentivirus and selected in 2 µg ml^{-1} puromycin for 7 d.

Sense sequences are as follows: control luciferase shRNA, 5′-CCGGCGCTGAGTACTTCGAAATGTCCTCGAGGACATTTCGAAGTACTCAGCGTTTTTG-3′; SHMT2 sh1, 5′-CCGGCCGGAGAGTTGTGGACTTTATCTCGAGATAAAGTCCACAACTCTCCGGTTTTTG-3′; SHMT2 sh2, 5′-CCGGGTCTGACGTCAAGCGGATATCCTCGAGGATATCCGCTTGACGTCAGACTTTTTG-3′; GLDC sh1, 5′-CCGGCCTGCCAACATCCGTTTGAAACTCGAGTTTCAAACGGATGTTGGCAGGTTTTTG-3′; GLDC sh2, 5′-CCGGCCACGGAAACTGCGATATTAACTCGAGTTAATATCGCAGTTTCCGTGGTTTTTG-3′; MAT2A sh1, 5′CCGGAGCAGTTGTGCCTGCGAAATACTCGAGTATTTCGCAGGCACAACTGCTTTTTTG-3′, MAT2A sh2, 5′-CCGGCCAGATAAGATTTGTGACCAACTCGAGTTGGTCACAAATCTTATCTGGTTTTTG-3′; MTHFR sh1, 5′-CCGGATATTAGACAGGACCATTATGCTCGAGCATAATGGTCCTGTCTAATATTTTTTG-3′, MTHFR sh2, 5′-CCGGAGAGTATCCAAGACGACATTCCTCGAGGAATGTCGTCTTGGATACTCTTTTTTT-3′; mat2a sh1, 5′-CCGGTTTGGAGGACGTACGTAATAACTCGAGTTATTACGT-ACGTCCTCCAAATTTTTG-3′ mat2a sh2, 5′-CCGGACCGGAATGAGGAAGATATTGCTCGAGCAATATCTTCCTCATTCCGGTTTTTTG-3′.

Immunoblotting. 1.5 × 10^6 cells were lysed in Laemmli-SDS buffer and sonicated. Total protein concentration was measured by Bradford assay. Total cell lysates were separated by SDS–PAGE and transferred to nitrocellulose, followed by blocking in 5% (vol/vol) milk in Tris-buffered saline with Tween-20, probing with the indicated antibodies and visualization by chemiluminescence (Roche). All primary antibody dilutions were at 1:1,000. Secondary antibody dilutions were at 1:5,000. The primary antibodies used were anti-β-actin[67] antibody (sc-47778), anti-GAPDH[68] antibody (sc-32233) and anti-goat-IgG HRP-linked secondary antibody (sc-2304) from Santa Cruz Biotechnology; anti-GLDC[24] antibody (ab97625), anti-histone H3[69] antibody (ab1791), anti-histone H3 (dimethyl K36)[70] antibody (ab9049), anti-MAT2A antibody (ab189208), anti-MTR[71] antibody (ab9209), anti-histone H3 (trimethyl K79)[72] antibody (ab2621), anti-MTHFR antibody (ab125707), anti-MTAP[73] antibody (ab55517) and anti-histone H4[74] antibody (ab7311) from Abcam; anti-histone H3 (trimethyl K4)[75] antibody (39159), anti-histone H3 (trimethyl K27)[76] antibody (39155), anti-histone H3 (trimethyl K36)[77] antibody (61101) and anti-histone H3 (trimethyl K9)[78] antibody (39765) from Active Motif; anti-β-catenin[79] antibody (BD610154) from BD Biosciences; anti-SHMT2[9] antibody (HPA020549) and anti-AHCY (SAHH) antibody (WH0000191M8) from Sigma; and anti-Symmetric Di-Methyl Arginine Motif[80] antibody (13222), anti-rabbit-IgG HRP-linked secondary antibody (7074P2) and anti-mouse-IgG HRP-linked secondary antibody (7076S) from Cell Signaling Technology.

Molecular cloning. The open-reading frame for human *MTHFR* was first cloned into the lentiviral expression plasmid PLVX-Tight. The modified doxycycline-inducible promoter sequence was replaced with a constitutive CMV promoter sequence to allow for constitutive expression of *MTHFR*. The open-reading frame for shRNA-resistant human *GLDC* was also cloned into the same modified PLVX-CMV construct.

Protein turnover experiments. 5 × 10^5 cells were treated with 20 µg ml^{-1} cycloheximide (Sigma) and collected for immunoblotting at indicated time points.

Analysis of α-ketoglutarate/succinate ratios. Analysis of intracellular α-ketoglutarate and succinate levels was performed by using BioVision kits (K677, K649) according to the manufacturer's recommendations.

Statistical analysis. GraphPad Prism (GraphPad Software) v7.0 was used for statistical analyses. No statistical methods were used to predetermine sample size. Statistical analysis in Fig. 1g,h and Extended Data Fig. 1k was carried out by using multiple t tests and statistical significance was corrected for multiple comparisons by using the Holm–Sidak method. Statistical analysis in Fig. 4c and Extended Data Fig. 4b was carried out by using paired Student's two-sided t tests. Statistical analysis in Fig. 4d and Extended Data Fig. 4c was performed by using chi-squared tests. Statistical analysis in Extended Data Figs. 2b and 5j was carried out by using unpaired Student's two-sided t tests. Statistical analysis in Fig. 2f and Extended Data Figs. 2f and 5l was carried out by using unpaired Student's two-sided t tests with Welch's correction. $P < 0.05$ was considered to be statistically significant. Significance levels and exact P values are indicated in relevant figure legends. Data were assumed to be normally distributed for all analyses conducted. Variances were not statistically different in any of the data. Data for independent experiments are presented as means ± s.d. unless otherwise stated.

Reporting Summary. Further information on research design is available in the Nature Research Reporting Summary linked to this article.

Data availability

The metabolomics datasets generated or analyzed during this study are included in this published article in Supplementary Tables 2 and 3. Additional datasets are also available from the corresponding author upon reasonable request. Source data are available online for Figs. 1–5 and Extended Data Figs. 1 and 3–5.

References

61. Kahlert, C. et al. Increased expression of ALCAM/CD166 in pancreatic cancer is an independent prognostic marker for poor survival and early tumour relapse. *Br. J. Cancer* **101**, 457–464 (2009).
62. Papal, S., Monti, C. E., Tennison, M. E. & Swaroop, A. Molecular dissection of cone photoreceptor-enriched genes encoding transmembrane and secretory proteins. *J. Neurosci. Res.* **97**, 16–28 (2019).
63. Wu, M. et al. Multiparameter metabolic analysis reveals a close link between attenuated mitochondrial bioenergetic function and enhanced glycolysis dependency in human tumor cells. *Am. J. Physiol Cell Physiol.* **292**, C125–C136 (2007).
64. Bligh, E. G. & Dyer, W. J. A rapid method of total lipid extraction and purification. *Can. J. Biochem. Physiol.* **37**, 911–917 (1959).
65. Smith, C. A., Want, E. J., O'Maille, G., Abagyan, R. & Siuzdak, G. XCMS: processing mass spectrometry data for metabolite profiling using nonlinear peak alignment, matching and identification. *Anal. Chem.* **78**, 779–787 (2006).
66. Alves, T. C. et al. Integrated, step-wise, mass-isotopomeric flux analysis of the TCA cycle. *Cell Metab.* **22**, 936–947 (2015).
67. Davis, M. A. et al. Calpain drives pyroptotic vimentin cleavage, intermediate filament loss, and cell rupture that mediates immunostimulation. *Proc. Natl Acad. Sci. USA* **116**, 5061–5070 (2019).
68. Zizza, P. et al. TRF2 positively regulates SULF2 expression increasing VEGF-A release and activity in tumor microenvironment. *Nucleic Acids Res.* https://doi.org/10.1093/nar/gkz041(2019).
69. Garcia-Lopez, S. et al. Deregulation of the imprinted *DLK1-DIO3* locus ncRNAs is associated with replicative senescence of human adipose-derived stem cells. *PloS One* **13**, e0206534 (2018).
70. Wang, L. et al. H3K36 trimethylation mediated by SETD2 regulates the fate of bone marrow mesenchymal stem cells. *PLoS Biol.* **16**, e2006522 (2018).
71. Fofou-Caillierez, M. B. et al. Interaction between methionine synthase isoforms and MMACHC: characterization in cblG-variant, cblG and cblC inherited causes of megaloblastic anaemia. *Hum. Mol. Genet.* **22**, 4591–4601 (2013).

72. Zhu, B. et al. The protective role of DOT1L in UV-induced melanomagenesis. *Nat. Commun.* **9**, 259 (2018).
73. Limm, K., Dettmer, K., Reinders, J., Oefner, P. J. & Bosserhoff, A. K. Characterization of the methylthioadenosine phosphorylase polymorphism rs7023954—incidence and effects on enzymatic function in malignant melanoma. *PloS One* **11**, e0160348 (2016).
74. Cooper, S. et al. Jarid2 binds mono-ubiquitylated H2A lysine 119 to mediate crosstalk between Polycomb complexes PRC1 and PRC2. *Nat. Commun.* **7**, 13661 (2016).
75. Chen, X., Zhi, X., Wang, J. & Su, J. RANKL signaling in bone marrow mesenchymal stem cells negatively regulates osteoblastic bone formation. *Bone Res.* **6**, 34 (2018).
76. Li, Y. et al. Genome-wide analyses reveal a role of Polycomb in promoting hypomethylation of DNA methylation valleys. *Genome Biol.* **19**, 18 (2018).
77. Fang, D., Gan, H., Wang, H., Zhou, H. & Zhang, Z. Probe the function of histone lysine 36 methylation using histone H3 lysine 36 to methionine mutant transgene in mammalian cells. *Cell Cycle* **16**, 1781–1789 (2017).
78. Zhang, X. et al. H3 ubiquitination by NEDD4 regulates H3 acetylation and tumorigenesis. *Nat. Commun.* **8**, 14799 (2017).
79. Freeman, T. J. et al. Inhibition of pannexin 1 reduces the tumorigenic properties of human melanoma cells. *Cancers* **11**, E102 (2019).
80. Gerhart, S. V. et al. Activation of the p53–MDM4 regulatory axis defines the anti-tumour response to PRMT5 inhibition through its role in regulating cellular splicing. *Sci. Rep.* **8**, 9711 (2018).
81. Sengupta, S. et al. Genome-wide expression profiling reveals EBV-associated inhibition of MHC class I expression in nasopharyngeal carcinoma. *Cancer Res.* **66**, 7999–8006 (2006).
82. Haslinger, C. et al. Microarray gene expression profiling of B-cell chronic lymphocytic leukemia subgroups defined by genomic aberrations and *VH* mutation status. *J. Clin. Oncol.* **22**, 3937–3949 (2004).
83. Zhang, J. et al. The genetic basis of early T-cell precursor acute lymphoblastic leukaemia. *Nature* **481**, 157–163 (2012).
84. Piccaluga, P. P. et al. Gene expression analysis of peripheral T cell lymphoma, unspecified, reveals distinct profiles and new potential therapeutic targets. *J. Clin. Invest.* **117**, 823–834 (2007).
85. Bonome, T. et al. A gene signature predicting for survival in suboptimally debulked patients with ovarian cancer. *Cancer Res.* **68**, 5478–5486 (2008).
86. Talantov, D. et al. Novel genes associated with malignant melanoma but not benign melanocytic lesions. *Clin. Cancer Res.* **11**, 7234–7242 (2005).
87. Wallace, T. A. et al. Tumor immunobiological differences in prostate cancer between African-American and European-American men. *Cancer Res.* **68**, 927–936 (2008).
88. Zhao, H. et al. Different gene expression patterns in invasive lobular and ductal carcinomas of the breast. *Mol. Biol. Cell* **15**, 2523–2536 (2004).

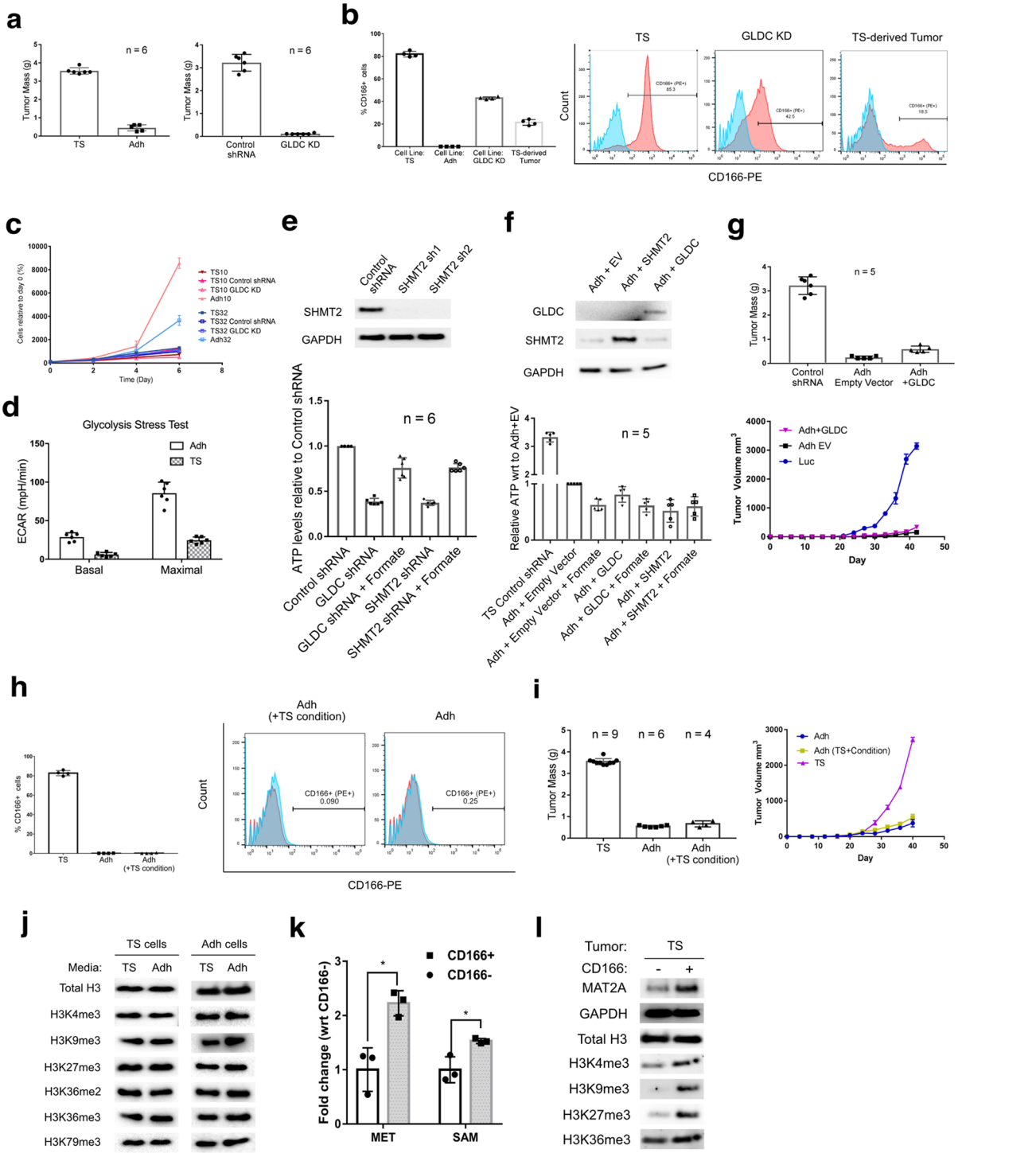

Extended Data Fig. 1 | Metabolomic characterization of lung tumor-initiating cells and differentiated cells. a, Mean tumor mass of implanted cells. Error bars, s.d.; $n=6$ tumors. **b**, Left, mean percentage of CD166$^+$ cells. Error bars, s.d.; $n=4$ biologically independent experiments. Right, representative flow cytometry plots, independently repeated four times. Unstained cells are in blue. **c**, Proliferation curves generated from mean cell viability. Error bars, s.d.; $n=6$ biologically independent experiments. **d**, Mean ECAR. Error bars, s.d.; $n=6$ biologically independent experiments. **e**,**f**, Top, immunoblots of the indicated cells, independently repeated three times. Bottom, mean ATP levels. Formate was supplemented at 0.5 mM. Error bars, s.d.; $n=6$ (**e**) and $n=5$ (**f**) biologically independent experiments. **g**, Top, mean tumor mass of implanted cells. Error bars, s.d.; $n=5$ tumors. Bottom, mean tumor volume. Error bars, s.e.m.; $n=4$ tumors. Mean tumor mass and volume for Control-knockdown (**a** and Fig. 1c) are included. **h**, Left, mean percentage of CD166$^+$ cells. Error bars, s.d.; $n=4$ biologically independent experiments. Right, representative flow cytometry plots, independently repeated four times. Unstained cells are in blue. **i**, Mean tumor mass and volume of implanted cells. Error bars, s.d. (left) and s.e.m. (right); $n=4$ tumors. Mean tumor mass and volume for TS and Adh cells (**a** and Fig. 1c) are included. **j**, Immunoblots of cells grown in the indicated conditions. Independent blots were repeated at least three times with similar results. Histone H3 is used as a loading control. **k**, Mean abundance of metabolites in cells sorted by CD166 expression from three different tumors. Error bars, s.d. *$P<0.05$, one-sided multiple *t* test corrected for multiple comparisons by the Holm–Sidak method. Exact *P* values (vs. CD166$^-$ cells) are as follows: methionine, 0.0102522; SAM, 0.01934. **l**, Immunoblots of sorted cells. Independent blots were repeated at least three times with similar results. GAPDH and total histone H3 were used as loading controls.

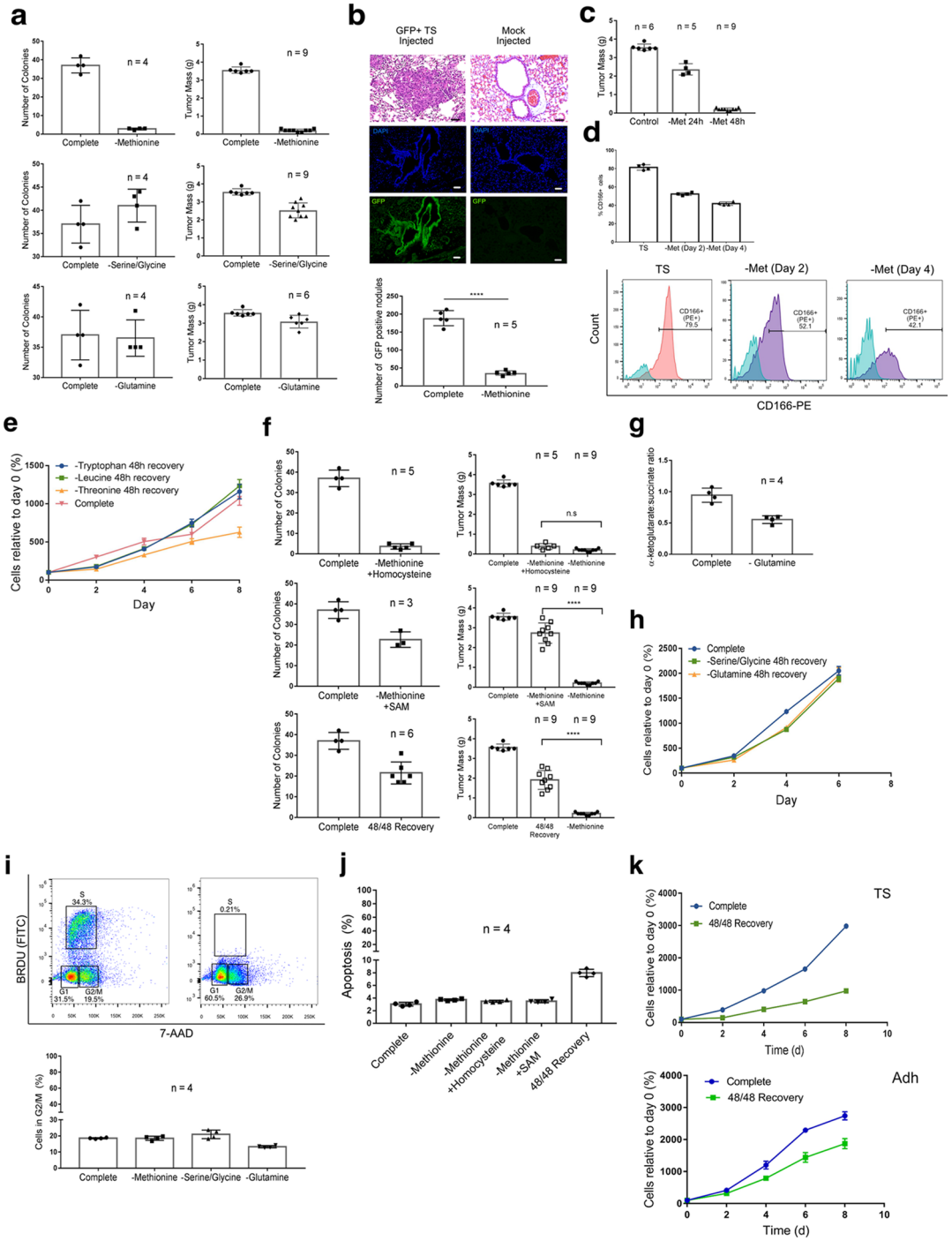

Extended Data Fig. 2 | The metabolic requirements of lung tumor-initiating cells. a, Left, mean number of colonies. Error bars, s.d.; $n=4$ biologically independent experiments. Right, mean tumor mass. Error bars, s.d.; $n=9$ (no methionine, no serine/glycine), $n=6$ (no glutamine) tumors. Mean TS tumor masses (Extended Data Fig. 1a) were included. **b**, Imaging experiments were independently repeated three times. Top, lesion from TS-implanted lung (l) and normal bronchiole (r). Black bars, 50 μm. Middle, GFP-positive lesion (l) and normal bronchiole (r). Scale bars, 40 μm. Bottom, mean number of GFP-positive lesions. Error bars, s.d.; $n=5$ lungs. ****$P<0.0001$ by unpaired two-sided Student's t test. **c**, Mean tumor mass. Error bars, s.d.; $n=5$ tumors. **d**, Top, mean percentage of CD166$^+$ cells. $n=4$ biologically independent experiments. Error bars, s.d. Bottom, representative flow cytometry plots independently repeated four times. Unstained cells are in blue. **e**, Proliferation curves generated from mean cell viability. Error bars, s.d.; $n=6$ biologically independent experiments. **f**, Left, mean number of colonies. Error bars, s.d.; $n=5$ (no methionine + homocysteine), $n=3$ (no methionine + SAM), $n=6$ (48/48) biologically independent replicates. Right, mean tumor mass. Error bars, s.d.; $n=9$ (no methionine + SAM, 48/48), $n=5$ (no methionine + homocysteine) tumors. Tumor masses for no methionine (**a**) and TS cells (Extended Data Fig. 1a) are included. ****$P<0.0001$, two-sided Student's t test with Welch's correction. P values (vs. no methionine): no methionine + homocysteine, 0.0505; no methionine + SAM, <0.0001; 48/48, <0.0001. **g**, Mean α-ketoglutarate/succinate ratios. Error bars, s.d.; $n=4$ biologically independent experiments. **h**, Proliferation curves generated from mean cell viability. Error bars, s.d.; $n=6$ biologically independent experiments. **i**, Top, representative flow cytometry plots independently repeated four times. Left, Complete condition. Right, Thymidine treated positive control. Bottom, mean percentage of cells in G2/M. Error bars, s.d.; $n=4$ biologically independent experiments. **j**, Mean percentage of Annexin V$^+$ cells. Error bars, s.d.; $n=4$ biologically independent experiments. **k**, Proliferation curves generated from mean cell viability. Error bars, s.d.; $n=6$ biologically independent experiments.

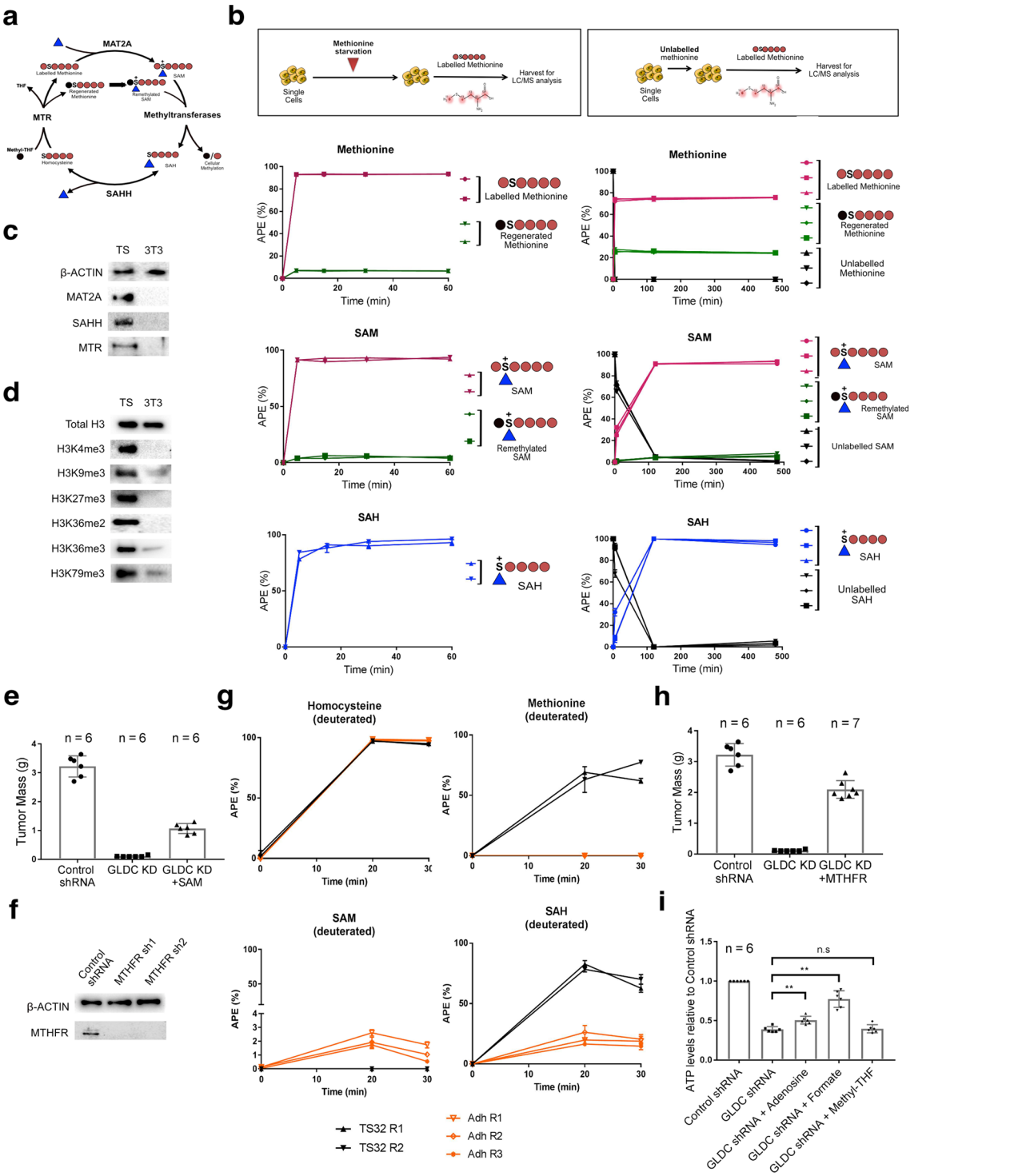

Extended Data Fig. 3 | Metabolic labeling and tracking of methionine cycle flux. a, Changes to [^{13}C]methionine through the methionine cycle. Red circles, ^{13}C; blue triangle, ATP; +, positive charge; black circle, ^{12}C; black letters, enzymes. **b**, Top, cells were starved of methionine (16 h; l) or not starved (r) before [^{13}C]methionine pulse–chase. Bottom, metabolite species detected are indicated on the right, and proportional abundance (% APE) is indicated on the left. Data represent the mean ± s.e.m.; $n = 3$ technical replicates. Technical replicates are shown to demonstrate technical consistency. $n = 2$ (bottom left) and $n = 3$ (bottom right) biologically independent experiments. **c**,**d**, Immunoblots of the indicated cells. β-actin (**c**) and total histone H3 (**d**) were used as loading controls. Independent blots were repeated at least three times with similar results. **e**, Mean tumor mass of implanted cells. Tumor masses from control- and *GLDC*-knockdown cells (Extended Data Fig. 1a) are included. Error bars, s.d.; $n = 6$ tumors. **f**, Immunoblots of the indicated lines. β-actin was used as a loading control. Independent blots were repeated at least three times with similar results. **g**, Percent APE of metabolite species derived from deuterated homocysteine. Data represent the mean ± s.e.m.; $n = 3$ technical replicates. Technical replicates are shown to demonstrate technical consistency. $n = 3$ biologically independent experiments. **h**, Mean tumor mass. Tumor masses from control- and *GLDC*-knockdown cells (Extended Data Fig. 1a) are included. Error bars, s.d.; $n = 7$ tumors. **i**, Mean ATP levels in the indicated cells supplemented with formate (0.5 mM), methyl-THF (20 μM) or adenosine (200 μM). Error bars, s.d.; $n = 6$ biologically independent experiments; $^{**}P < 0.005$, Student's two-sided *t* test with Welch's correction. Exact *P* values (vs. *GLDC* shRNA) are as follows: *GLDC* shRNA + methyl-THF, 0.7947; *GLDC* shRNA + adenosine, 0.0011; *GLDC* shRNA + formate, 0.0010.

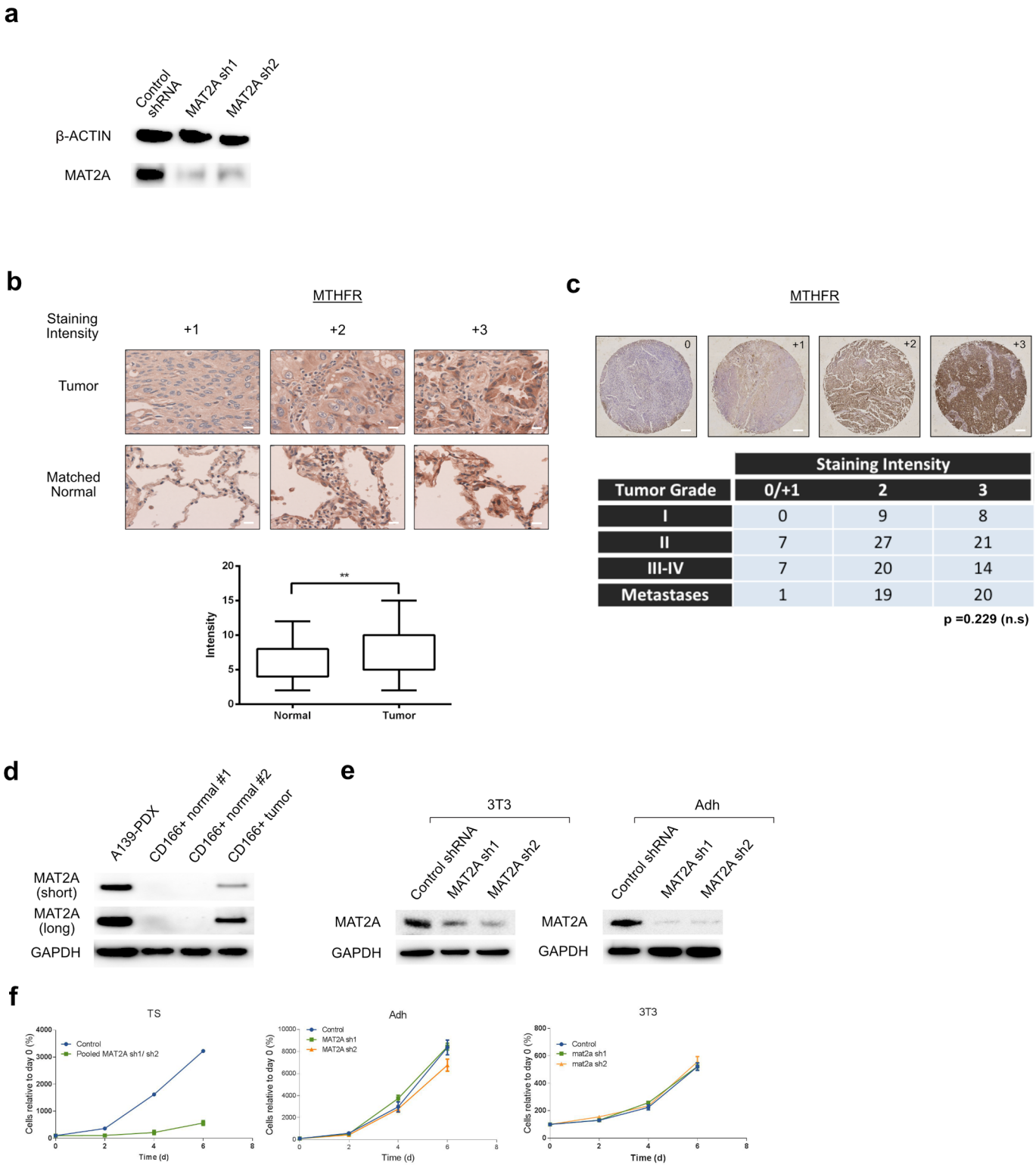

Extended Data Fig. 4 | Functional and clinical relevance of methionine cycle enzymes in NSCLC. a, Immunoblots of the indicated enzymes. β-actin was used as a loading control. Independent blots were repeated at least three times with similar results. **b**, MTHFR immunohistochemistry (performed once) of a tumor microarray ($n=47$) containing paired tumor and normal sections. Top, representative staining intensity. White bar, 20 μm. Bottom, box-and-whisker plots comparing the intensity of tumor and normal sections. Intensity was defined as the product of the maximum immunostaining intensity and the percentage of tumor cells stained per section. Box, twenty-fifth to seventy-fifth percentile; the median value coincides with the seventy-fifth percentile; whiskers indicate the minima and maxima. $^{**}P=0.0005$, paired Student's two-sided t test. $t=3.776$, d.f. = 46. **c**, MTHFR immunohistochemistry (performed once) of an NSCLC tumor microarray ($n=153$). Top, representative staining intensity. White bar, 200 μm. Bottom, contingency table correlating staining intensity with NSCLC grade. Chi-squared test P value ($P=0.2297$) is indicated at the bottom right. $\chi^2=8.116$, d.f. = 6. **d**,**e**, Immunoblots of MAT2A in the indicated cells or tumors. GAPDH was used as a loading control. Independent blots were repeated at least three times with similar results. **f**, Proliferation curves generated from mean cell viability of the indicated lines. Error bars, s.d.; $n=10$ biologically independent experiments.

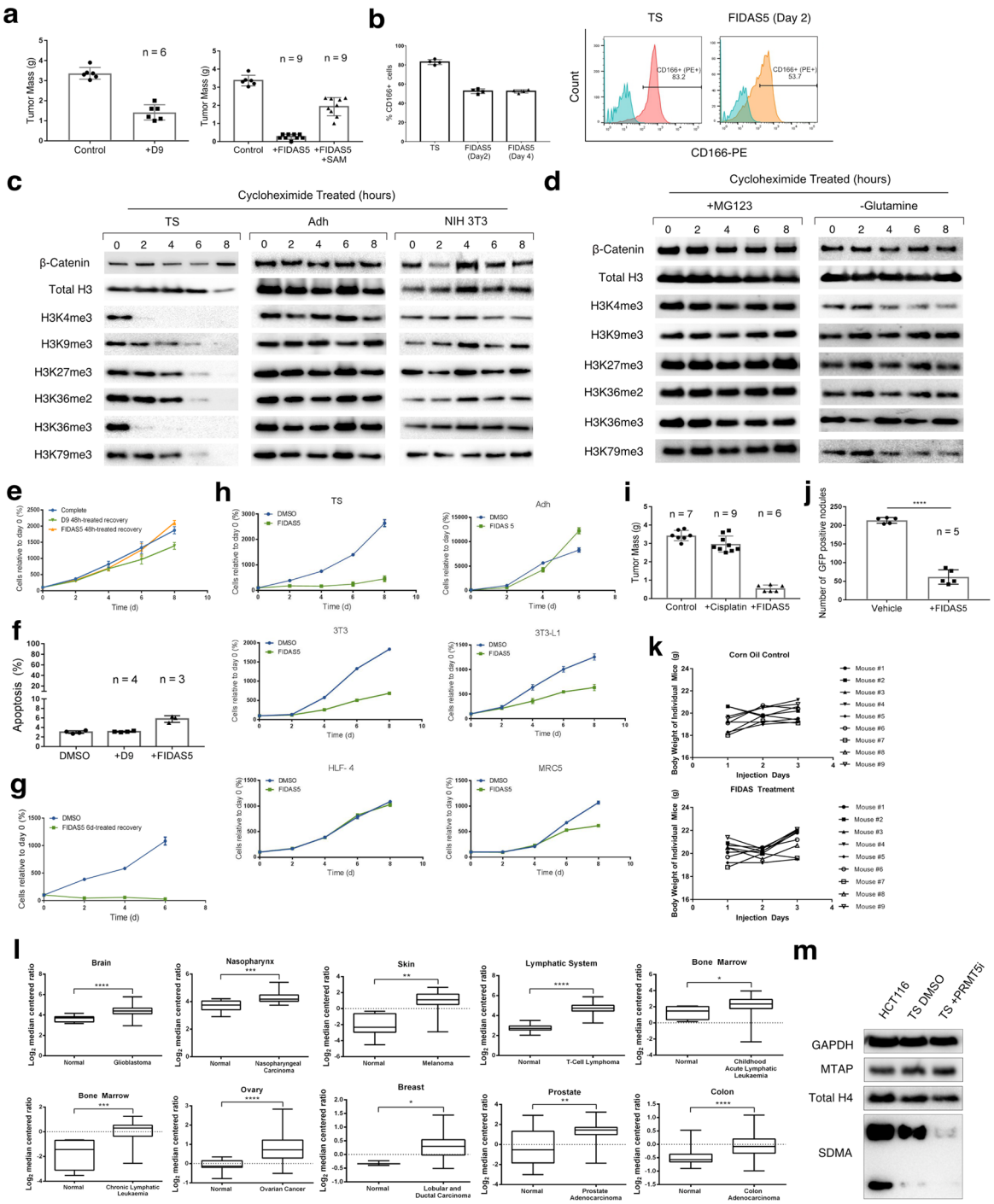

Extended Data Fig. 5 | Small-molecule inhibition of the methionine cycle disrupts the tumorigenicity of lung tumor-initiating cells. a, Mean tumor mass of implanted cells. Error bars, s.d.; $n=6$ (D9, DMSO), $n=9$ (FIDAS, FIDAS + SAM) tumors. **b**, Left, mean percentage of CD166$^+$ cells. Error bars, s.d.; $n=4$ biologically independent experiments. Right, representative flow cytometry plots independently repeated four times. Unstained cells are in blue. **c**,**d**, Immunoblots of the indicated cells. β-catenin was used as a loading control. Independent blots were repeated at least three times with similar results. **e**, Proliferation curves generated from mean cell viability. Error bars, s.d.; $n=10$ biologically independent experiments. **f**, Mean percentage of Annexin V$^+$ cells. Error bars, s.d.; $n=4$ (DMSO, D9), $n=3$ (FIDAS) biologically independent experiments. **g**,**h**, Proliferation curves generated from mean cell viability. Error bars, s.d.; $n=10$ biologically independent experiments. **i**, Mean tumor mass of implanted cells. Error bars, s.d.; $n=7$ (control), $n=6$ (FIDAS) and $n=9$ (cisplatin) tumors. **j**, Mean number of GFP$^+$ lesions. Error bars, s.d.; $n=5$ lungs. $^{****}P<0.0001$, two-sided unpaired Student's t test. **k**, Individual weight plots of nine mice undergoing the indicated treatment. **l**, Mean *MAT2A* mRNA levels in normal versus tumor tissue, including glioblastoma (TCGA), colorectal cancer (TCGA), nasopharyngeal carcinoma[81], leukemia[82,83], lymphoma[84], ovarian carcinoma[85], melanoma[86], prostate adenocarcinoma[87] and breast cancer[88]. $^{****}P<0.0001$, $^{***}P<0.001$, $^{**}P\leq0.01$, $^{*}P\leq0.05$, Student's unpaired two-sided t test with Welch's correction. P values and numbers of normal and tumor samples are as follows: brain: $P<0.0001$; $n=10$ and $n=547$; nasopharynx, $P=0.0005$; $n=10$ and $n=31$; skin: $P=0.0015$; $n=7$ and $n=63$; lymphatic system, $P<0.0001$; $n=20$ and $n=40$; bone marrow (childhood acute lymphatic leukemia): $P=0.0492$; $n=8$ and $n=566$; bone marrow (chronic lymphatic leukemia): $P=0.0003$; $n=11$ and $n=100$; ovary: $P<0.0001$; $n=10$ and $n=185$; breast, $P=0.0215$; $n=5$ and $n=59$; prostate: $P=0.0010$; $n=20$ and $n=69$; colon: $P<0.0001$; $n=22$ and $n=215$. **m**, Immunoblots of the indicated cells. Independent blots were repeated at least three times with similar results.

nature research

Corresponding author(s): Wai Leong Tam

Last updated by author(s): Apr 12, 2019

Reporting Summary

Nature Research wishes to improve the reproducibility of the work that we publish. This form provides structure for consistency and transparency in reporting. For further information on Nature Research policies, see Authors & Referees and the Editorial Policy Checklist.

Statistics

For all statistical analyses, confirm that the following items are present in the figure legend, table legend, main text, or Methods section.

n/a	Confirmed	
☐	☒	The exact sample size (*n*) for each experimental group/condition, given as a discrete number and unit of measurement
☐	☒	A statement on whether measurements were taken from distinct samples or whether the same sample was measured repeatedly
☐	☒	The statistical test(s) used AND whether they are one- or two-sided *Only common tests should be described solely by name; describe more complex techniques in the Methods section.*
☒	☐	A description of all covariates tested
☒	☐	A description of any assumptions or corrections, such as tests of normality and adjustment for multiple comparisons
☐	☒	A full description of the statistical parameters including central tendency (e.g. means) or other basic estimates (e.g. regression coefficient) AND variation (e.g. standard deviation) or associated estimates of uncertainty (e.g. confidence intervals)
☐	☒	For null hypothesis testing, the test statistic (e.g. *F*, *t*, *r*) with confidence intervals, effect sizes, degrees of freedom and *P* value noted *Give P values as exact values whenever suitable.*
☒	☐	For Bayesian analysis, information on the choice of priors and Markov chain Monte Carlo settings
☒	☐	For hierarchical and complex designs, identification of the appropriate level for tests and full reporting of outcomes
☒	☐	Estimates of effect sizes (e.g. Cohen's *d*, Pearson's *r*), indicating how they were calculated

Our web collection on statistics for biologists contains articles on many of the points above.

Software and code

Policy information about availability of computer code

Data collection	BD FACSDiva Software version 6.0 for flow cytometry data collection Image Lab 5.2.1 for viewing and processing of Western Blot images Zeiss Observer D1 was used for immnuofluorescence analysis, the accompanying Zeiss AxioVision Release 4.8.2 software was used to capture the resultant images.
Data analysis	Graphpad Prism (Graphpad Software) v 7.0 was used for statistical analyses. FlowJo Version 10.1 was used to analyze flow cytometry data XCMS: version 1.30.3 (Scripps Institute) and TargetLynx module in MassLynx software (version 4.1 SCN810, Waters Corp) was used to analyze Mass Spectrometry Data

For manuscripts utilizing custom algorithms or software that are central to the research but not yet described in published literature, software must be made available to editors/reviewers. We strongly encourage code deposition in a community repository (e.g. GitHub). See the Nature Research guidelines for submitting code & software for further information.

Data

Policy information about availability of data

All manuscripts must include a data availability statement. This statement should provide the following information, where applicable:

- Accession codes, unique identifiers, or web links for publicly available datasets
- A list of figures that have associated raw data
- A description of any restrictions on data availability

Correspondence and requests for materials should be addressed to B.L (bing.lim@merck.com) or W.L.T (tamwl@gis.a-star.edu.sg). The metabolomics datasets generated or analyzed during this study are included in this published article in Supplementary Tables 2 and 3. Additional datasets are also available from the corresponding author on reasonable request.

Field-specific reporting

Please select the one below that is the best fit for your research. If you are not sure, read the appropriate sections before making your selection.

☒ Life sciences ☐ Behavioural & social sciences ☐ Ecological, evolutionary & environmental sciences

For a reference copy of the document with all sections, see nature.com/documents/nr-reporting-summary-flat.pdf

Life sciences study design

All studies must disclose on these points even when the disclosure is negative.

Sample size	For all Experiments at least 3 or more replicates was used in order to obtain statistical significance. For all animal studies, at least 3 animals were used for each experimental group; this is specified in the figure legends.
Data exclusions	No data was excluded from the analysis
Replication	All experiments were replicated at least 3 times using the same experimental conditions. In the case of knockdown experiments, two or more shRNAs were used per gene target. All replication attempts were successful.
Randomization	4-6 week old mice were randomly selected in animal experiments. There was no sex bias in our selection of mice.
Blinding	IHCs performed on tumor microarrays was done in a blinded fashion, where the researcher was unaware of the tumor stage of the individual tumor section.

Reporting for specific materials, systems and methods

We require information from authors about some types of materials, experimental systems and methods used in many studies. Here, indicate whether each material, system or method listed is relevant to your study. If you are not sure if a list item applies to your research, read the appropriate section before selecting a response.

Materials & experimental systems

n/a	Involved in the study
☐	☒ Antibodies
☐	☒ Eukaryotic cell lines
☒	☐ Palaeontology
☐	☒ Animals and other organisms
☐	☒ Human research participants
☒	☐ Clinical data

Methods

n/a	Involved in the study
☒	☐ ChIP-seq
☐	☒ Flow cytometry
☒	☐ MRI-based neuroimaging

Antibodies

Antibodies used

All antibodies are used at 1:1000 dilution unless otherwise stated.

Supplier: Santa Cruz
anti-β-Actin mouse monoclonal clone C4 (sc-47778). Lot no: G0213
anti-GAPDH mouse monoclonal clone 6C5 (sc-32233). Lot no: F2712
Donkey anti-goat secondary antibody, conjugated with HRP-(sc-2304) Lot no: F1803. Dilution 1:5000

Supplier: Abcam
anti-GLDC rabbit polyclonal (ab97625). Lot no: GR277520-6
anti-H3 rabbit polyclonal (ab1791). Lot no: GR150473-1
anti-H3(dimethylK36) rabbit polyclonal (ab9049). Lot No: GR75522-3
anti MAT2A rabbit polyclonal (ab189208). Lot no: GR179402-12
anti MTR goat polyclonal (ab9209). Lot no: GR65779-8
anti-H3(trimethylK79) rabbit polyclonal (ab2621). Lot no: GR188147-1
anti MTHFR rabbit polyclonal (ab125707). Lot no: GR289909-1
Anti-GFP chicken polyclonal (ab13970). Lot no: GR236651-10
Anti-Histone H4 rabbit polyclonal (ab 7311). Lot no: GR325224-1
Anti-MTAP mouse monoclonal (ab 55517). Lot no: GR305460-1

Supplier: Active Motif
anti H3(trimethyl K4) rabbit polyclonal (39915). Lot no: 12613005

anti H3(trimethyl K27) rabbit polyclonal (39155). Lot no: 12912013
anti-H3(trimethylK36) rabbit polyclonal (61101). Lot no: 12912002
anti-H3(trimethylK9) rabbit polyclonal (39765). Lot no: 31610002

Supplier: BD Biosciences
anti-β-catenin mouse monoclonal Clone 14/Beta-Catenin (BD610154). Lot no: 6176992

Supplier: Genetex
anti-MAT2A mouse monoclonal Clone AT3A2 (GTX50027). Lot no: 821803570

Supplier: Sigma
Anti-MAT2A rabbit polyclonal (HPA043028). Lot no:R40523
Anti-SHMT2 rabbit polyclonal (HPA020549). Lot no: P09754
Anti-AHCY mouse monoclonal antibody clone M1, (WH0000191M8). Lot no:08183-M1
Anti-CD166/ALCAM rabbit polyclonal (HPA010926). Lot no:B75231

Supplier: R&D Biosystems
Anti ALCAM-PE conjugate clone 105902 (FAB6561P). Lot no: LAR0413011

Supplier: CST
Anti-Symmetric Di-Methyl Arginine Motif rabbit monoclonal (13222). Lot no: 1.
Goat anti-rabbit IgG, HRP-linked Antibody (7074P2). Lot no: 25. Dilution 1:5000
Goat anti-mouse IgG, HRP-linked Antibody (7076S). Lot no: 33. Dilution 1:5000

Supplier: Thermofisher
Goat anti-Chicken IgY (H+L) Secondary Antibody, Alexa Fluor 488. Polyclonal (A-11039). Lot no: 1759025
Donkey anti-Mouse IgG (H+L) Secondary Antibody, Alexa Fluor 594. Polyclonal (A21203). Lot no: 1820027
Goat anti-Rabbit IgG (H+L) Secondary Antibody, Alexa Fluor 647. Polyclonal (A21245). Lot no: 1558736

Validation

Previously published antibodies are cited in the Methods section and below. Human and species cross-reactivity was determined by Western Blots. Manufacturer validation statements of specific antibodies are stated below.
MTHFR antibody was validated by us in IHC and shRNA knockdown experiments using TS cell lysates in Extended Figures 4b and 3f.
Sigma AHCY (SAHH,WH0000191M8) was validated by us in WB experiments using TS cell lysates in Figure 1i.
Sigma MAT2A antibody (HPA043028) was validated by us in IHC experiments in Figures 4b and 4c.
Genetex MAT2A antibody (GTX50027) was validated by us in immunofluorescence (IF) experiments in Figures 4e.
MAT2A antibody (ab 189208) was validated by us in shRNA knockdown experiments in TS cell lysates in Extended Figure 4a.

Supplier: Santa Cruz
anti-β-Actin(1) mouse monoclonal clone C4 (sc-47778). Detects human and mouse β-Actin by WB, IP, IF, IHC(P) and ELISA .
anti-GAPDH(2) mouse monoclonal clone 6C5 (sc-32233). Detects human and mouse GAPDH by WB, IP, and IF.
Donkey anti-goat secondary antibody, conjugated with HRP-(sc-2304) Manufacturer validates detection of goat IgG by WB.

Supplier: Abcam
anti-GLDC(3) rabbit polyclonal (ab97625). Manufacturer validates detection of human GLDC by WB, ICC/IF.
anti-H3(4) rabbit polyclonal (ab1791). Manufacturer validates detection of human and mouse H3 by WB.
anti-H3(dimethylK36)(5) rabbit polyclonal (ab9049). Manufacturer validates detection of human H3 and mouse (dimethylK36) by WB.
anti MAT2A rabbit polyclonal (ab189208). Manufacturer validates detection of human and mouse MAT2A by WB. Validated by us in shRNA knockdown experiments in TS cell lysates in Extended Figure 4a
anti MTR(6) goat polyclonal (ab9209). Manufacturer validates detection of human MTR by WB and IHC-P.
anti-H3(trimethylK79)(7) rabbit polyclonal (ab2621). Manufacturer validates detection of human and mouse H3(trimethylK79) by ICC/IF, ChIP, WB, ChIP/Chip.
anti MTHFR rabbit polyclonal (ab125707) Manufacturer validates detection of human and mouse MTHFR by WB (manufacturer). MTHFR antibody was validated by us in IHC and shRNA knockdown experiments in TS cell lysates in Extended Figures 4b and 3f.
Anti-GFP(8) chicken polyclonal (ab13970). Manufacturer validates detection of GFP by IF.
Anti-Histone H4(9) rabbit polyclonal (ab 7311) Manufacturer validates detection of human and mouse H4 by WB.
Anti-MTAP(10) mouse monoclonal (ab 55517) Manufacturer validates detection of human MTAP by WB.

Supplier: Active Motif
anti H3(trimethyl K4)(11) rabbit polyclonal (39915). Manufacturer validates detection of human and mouse H3(trimethyl K4) by WB.
anti H3(trimethyl K27)(12) rabbit polyclonal (39155). Manufacturer validates detection of human and mouse H3(trimethyl K27) by WB.
anti-H3(trimethylK36)(13) rabbit polyclonal (61101). Manufacturer validates detection of human and mouse H3(trimethylK36) by WB.
anti-H3(trimethylK9)(14) rabbit polyclonal (39765). Manufacturer validates detection of human and mouse H3(trimethylK9) by WB.

Supplier: BD Biosciences
anti-β-catenin(15) mouse monoclonal Clone 14/Beta-Catenin (BD610154). Manufacturer validates detection of human and mouse β-catenin by WB.

Supplier: Genetex

anti-MAT2A(16) mouse monoclonal Clone AT3A2 (GTX50027). Manufacturer validates detection of human MAT2A by WB and IHC-P. Validated by us in immunofluorescence (IF) experiments in Figure 4e.

Supplier: Sigma
Anti-MAT2A rabbit polyclonal (HPA043028). Manufacturer validates detection of human MAT2A by IHC in the Human Protein Atlas. Validated by us in IHC experiments in Figures 4b and 4c
Anti-SHMT2(17) rabbit polyclonal (HPA020549). Manufacturer validates detection of human SHMT2 by WB.
Anti-SAHH mouse monoclonal antibody clone M1, (WH0000191M8). Manufacturer validates detection of human SAHH by WB. Validated by us in WB experiments using TS cell lysates in Figure 1i
Anti-CD166/ALCAM(18) rabbit polyclonal (HPA010926). Manufacturer validates detection of human CD166/ALCAM by IHC in the Human Protein Atlas.

Supplier: R&D Biosystems
Anti ALCAM-PE(3) conjugate clone 105902 (FAB6561P). Manufacturer validates detection of human CD166/ALCAM for flow-cytometry.

Supplier: CST
Anti-Symmetric Di-Methyl Arginine Motif(19) rabbit monoclonal (13222). Manufacturer validates detection of human SDMA for WB.
Goat anti-rabbit IgG, HRP-linked Antibody (7074P2). Manufacturer validates detection of rabbit IgG in WB.
Goat anti-mouse IgG, HRP-linked Antibody (7076S). Manufacturer validates detection of rabbit IgG in WB.

Supplier: Thermofisher
Goat anti-Chicken IgY (H+L) Secondary Antibody, Alexa Fluor 488. Polyclonal (A-11039). Manufacturer validates use in IF.
Donkey anti-Mouse IgG (H+L) Secondary Antibody, Alexa Fluor 594. Polyclonal (A21203). Manufacturer validates use in IF.
Goat anti-Rabbit IgG (H+L) Secondary Antibody, Alexa Fluor 647. Polyclonal (A21245). Manufacturer validates use in IF.

References:
1. Davis, M.A., et al. Calpain drives pyroptotic vimentin cleavage, intermediate filament loss, and cell rupture that mediates immunostimulation. Proceedings of the National Academy of Sciences of the United States of America (2019).
2. Zizza, P., et al. TRF2 positively regulates SULF2 expression increasing VEGF-A release and activity in tumor microenvironment. Nucleic Acids Res (2019).
3. Zhang, W.C., et al. Glycine decarboxylase activity drives non-small cell lung cancer tumor-initiating cells and tumorigenesis. Cell 148, 259-272 (2012).
4. Garcia-Lopez, S., et al. Deregulation of the imprinted DLK1-DIO3 locus ncRNAs is associated with replicative senescence of human adipose-derived stem cells. PloS one 13, e0206534 (2018).
5. Wang, L., et al. H3K36 trimethylation mediated by SETD2 regulates the fate of bone marrow mesenchymal stem cells. PLoS Biol 16, e2006522 (2018).
6. Fofou-Caillierez, M.B., et al. Interaction between methionine synthase isoforms and MMACHC: characterization in cblG-variant, cblG and cblC inherited causes of megaloblastic anaemia. Hum Mol Genet 22, 4591-4601 (2013).
7. Zhu, B., et al. The protective role of DOT1L in UV-induced melanomagenesis. Nat Commun 9, 259 (2018).
8. Papal, S., Monti, C.E., Tennison, M.E. & Swaroop, A. Molecular dissection of cone photoreceptor-enriched genes encoding transmembrane and secretory proteins. J Neurosci Res 97, 16-28 (2019).
9. Cooper, S., et al. Jarid2 binds mono-ubiquitylated H2A lysine 119 to mediate crosstalk between Polycomb complexes PRC1 and PRC2. Nat Commun 7, 13661 (2016).
10. Limm, K., Dettmer, K., Reinders, J., Oefner, P.J. & Bosserhoff, A.K. Characterization of the Methylthioadenosine Phosphorylase Polymorphism rs7023954 - Incidence and Effects on Enzymatic Function in Malignant Melanoma. PloS one 11, e0160348 (2016).
11. Chen, X., Zhi, X., Wang, J. & Su, J. RANKL signaling in bone marrow mesenchymal stem cells negatively regulates osteoblastic bone formation. Bone Res 6, 34 (2018).
12. Li, Y., et al. Genome-wide analyses reveal a role of Polycomb in promoting hypomethylation of DNA methylation valleys. Genome Biol 19, 18 (2018).
13. Fang, D., Gan, H., Wang, H., Zhou, H. & Zhang, Z. Probe the function of histone lysine 36 methylation using histone H3 lysine 36 to methionine mutant transgene in mammalian cells. Cell Cycle 16, 1781-1789 (2017).
14. Zhang, X., et al. H3 ubiquitination by NEDD4 regulates H3 acetylation and tumorigenesis. Nat Commun 8, 14799 (2017).
15. Freeman, T.J., et al. Inhibition of Pannexin 1 Reduces the Tumorigenic Properties of Human Melanoma Cells. Cancers (Basel) 11(2019).
16. Zhang, W., et al. Fluorinated N,N-dialkylaminostilbenes repress colon cancer by targeting methionine S-adenosyltransferase 2A. ACS chemical biology 8, 796-803 (2013).
17. Kim, D., et al. SHMT2 drives glioma cell survival in ischaemia but imposes a dependence on glycine clearance. Nature 520, 363-367 (2015).
18. Kahlert, C., et al. Increased expression of ALCAM/CD166 in pancreatic cancer is an independent prognostic marker for poor survival and early tumour relapse. Br J Cancer 101, 457-464 (2009).
19. Gerhart, S.V., et al. Activation of the p53-MDM4 regulatory axis defines the anti-tumour response to PRMT5 inhibition through its role in regulating cellular splicing. Scientific reports 8, 9711 (2018).

Eukaryotic cell lines

Policy information about cell lines

Cell line source(s)	Tumor sphere lines were derived by us from freshly resected human non-small cell lung cancer patient samples. Adh and GLDC KD lines were further derived from Tumor sphere lines. All other human cancer and murine cell lines (NIH 3T3, NIH

	3T3-L1, HLF, MRC-5,PC-9, OVCAR-5, HT-29, SW 480, CACO-2, HCT-116, MCF-7, MDA-MB-436 and SUM-159) were obtained from ATCC.
Authentication	Tumor sphere lines were derived from us from human primary tissue samples. We confirmed their origin and cell type by human protein expression analysis and genomic exon-sequencing analysis (See Supplementary Table 1). All other human cancer and murine cell lines were obtained from ATCC, and not directly authenticated by us.
Mycoplasma contamination	All cell lines were tested regularly (e.g, every 6 months for mycoplasma contamination) and results were negative.
Commonly misidentified lines (See ICLAC register)	No commonly misidentified cell lines were used.

Animals and other organisms

Policy information about studies involving animals; ARRIVE guidelines recommended for reporting animal research

Laboratory animals	4-6 weeks male and female NOD.Cg-Prkdc(scid) Il2rg(tm1wjl) SzJ (Jackson Laboratories). Mice were randomly allocated and not selected by sex or age into experimental groups.
Wild animals	Study did not involve wild animals.
Field-collected samples	Study did not involve field-collected samples.
Ethics oversight	All animal experiments were approved by the Agency for Science Technology and Research Singapore – Biological Resource Centre IACUC (Protocol number 171286). The use of patient derived xenografts (PDX) has been approved by the SingHealth Centralised Institutional Review Board (CIRB Ref: 2007/444/B).

Note that full information on the approval of the study protocol must also be provided in the manuscript.

Human research participants

Policy information about studies involving human research participants

Population characteristics	Relevant clinical information is provided in Supplementary Table 1.
Recruitment	Written informed consent was obtained from all participating patients diagnosed with Non-Small Cell Adenocarcinoma prior to surgical resection or biopsy. Clinical material was then used to derive patient derived xenografts in immunocompromised mice. Self selection bias is unlikely to be present and is unlikely to affect downstream results.
Ethics oversight	The use of patient derived xenografts (PDX) has been approved by the SingHealth Centralised Institutional Review Board (CIRB Ref: 2007/444/B).

Note that full information on the approval of the study protocol must also be provided in the manuscript.

Flow Cytometry

Plots

Confirm that:

☒ The axis labels state the marker and fluorochrome used (e.g. CD4-FITC).

☒ The axis scales are clearly visible. Include numbers along axes only for bottom left plot of group (a 'group' is an analysis of identical markers).

☒ All plots are contour plots with outliers or pseudocolor plots.

☒ A numerical value for number of cells or percentage (with statistics) is provided.

Methodology

Sample preparation	Human tumor sphere cells previously derived from patient xenografts were used. These cells were first dissociated with accutase prior to analysis. For human patient sample derived PDX cells, , tumors were harvested in cold PBS with antibiotics, chopped with a sterile blade and incubated in 1mg/ml collagenase/dispase (Sigma Aldrich) in DMEM/F12 media (Thermo Fisher Scientific) at 37 °C with agitation. Suspensions were then washed in PBS and passed through 70 and 40 µm cell strainers, centrifuged and evaluated for cell viability by tryphan blue exclusion before downstream assays. Dissociated cells were stained with antibodies conjugated with PE against human CD166 (R&D Systems FAB6561P) in DPBS containing 5 % FBS for 1 hour at 4°C. Cells were then washed and resuspended in DPBS. The fluorescence intensity was measured on a flow cytometer (BD LSR II). Cell sorting was performed on a FACSAria II (BD).
Instrument	SRII (BD) for cytometry. FACSARiall (BD) for FACS sorting
Software	Collection: BD FACSDiva Software version 6.0 Analysis: Flowjo 10.1

Cell population abundance	%CD166+ cells within tumors were reported in Supplementary Figures and FIgures. The purity was verified by flow cytometry. and sorted cells were immediately used for downstream analysis.
Gating strategy	Refer to Supplementary Figure 1 for gating strategy. An 'Unstained' sample is used as a negative control.

☒ Tick this box to confirm that a figure exemplifying the gating strategy is provided in the Supplementary Information.